

# Oxygen Surface Exchange Kinetics and Stability of (La,Sr)<sub>2</sub>CoO<sub>4±δ</sub>/La<sub>1-x</sub>Sr<sub>x</sub>MO<sub>3-δ</sub> (M = Co and Fe) Hetero-interfaces at Intermediate Temperatures

Dongkyu Lee<sup>1,2,+</sup>, Yueh-Lin Lee<sup>1,2,+</sup>, Wesley T. Hong<sup>1,3</sup>, Michael D. Biegalski<sup>4</sup>, Dane Morgan<sup>5,\*</sup>,  
and Yang Shao-Horn<sup>1,2,3,\*</sup>

<sup>1</sup>*Electrochemical Energy Laboratory, <sup>2</sup>Department of Mechanical Engineering, and <sup>3</sup>Department of Materials Science and Engineering, Massachusetts Institute of Technology, 77 Massachusetts Avenue, Cambridge, Massachusetts 02139, United States*

<sup>4</sup>*Center for Nanophase Materials Sciences, Oak Ridge National Laboratory, Oak Ridge, Tennessee 37831, United States*

<sup>5</sup>*Department of Materials Science and Engineering, University of Wisconsin–Madison, 1509 University Avenue, Madison, Wisconsin 53706, United States*

## Abstract

Heterostructured oxide interfaces created by decorating Ruddlesden-Popper (RP) phases on  $ABO_3$  perovskites have shown not only pronounced cation segregation at the interface and in the RP phase but also enhanced kinetics for oxygen electrocatalysis at elevated temperatures. In this study, combining experimental and theoretical approaches, we report and compare the time-dependent surface exchange kinetics and stability of  $(La_{0.5}Sr_{0.5})_2CoO_{4\pm\delta}$  ( $LSC_{214}$ )-decorated  $La_{0.6}Sr_{0.4}Co_{0.2}Fe_{0.8}O_{3-\delta}$  ( $LSCF_{113}$ ) and  $La_{0.8}Sr_{0.2}CoO_{3-\delta}$  ( $LSC_{113}$ ) thin films. While  $LSC_{214}$  decoration on  $LSC_{113}$  greatly reduced the degradation in the surface exchange kinetics as a function of time relative to undecorated  $LSC_{113}$ ,  $LSCF_{113}$  with  $LSC_{214}$  coverage showed comparable surface exchange kinetics and stability relative to undecorated  $LSCF_{113}$ . This difference is attributed to stabilization of  $LSC_{113}$  surface by  $LSC_{214}$  decoration and greater stability of  $LSCF_{113}$  against decomposition into secondary phases than  $LSC_{113}$ . This hypothesis is supported by density functional theory (DFT) computation, revealing greater surface Sr segregation for  $LSCF_{113}$ , which is predicted to have an SrO termination, than  $LSC_{113}$ , which is predicted to have a less Sr enriched  $(La_{0.25}Sr_{0.75})O$  termination. Furthermore, DFT also showed a lower energy gain to move Sr from  $LSCF_{113}$  into  $LSC_{214}$  relative to the  $LSC_{214}$ - $LSC_{113}$  surface, and predicted the stability of  $LSCF_{113}$ ,  $LSC_{113}$ , and  $LSC_{214}$  with 100% Sr substitution in their top (001) surface. The stability differences of Sr substitution (with La) in  $LSCF_{113}$ ,  $LSC_{113}$ , and  $LSC_{214}$ , along with the assessed DFT decomposition free energies of fully Sr substituted  $LSCF_{113}$ ,  $LSC_{113}$ , and  $LSC_{214}$ , correlate with experimental observation of surface stability trends in surface particle formation of  $LSCF_{113}$  and  $LSC_{113}$  without and with  $LSC_{214}$  decoration.

## Keywords

fuel cells, heterostructure interface, oxygen surface exchange kinetics, long-term stability, surface chemistry, cation interdiffusion, surface stability, density functional theory

## 1. Introduction

The majority of efficiency loss in lower-temperature solid oxide fuel cells (SOFCs) results from slow oxygen reduction reaction (ORR) kinetics at the cathode.<sup>1-3</sup> Lanthanum strontium manganite (LSM)<sup>4-8</sup> alloys are currently utilized as a cathode material and operate efficiently only at high temperatures such as 1000 °C. Therefore, there is a need to search for electrode materials with high catalytic activity, particularly for intermediate temperatures (500 – 700 °C) SOFCs. Mixed ionic and electronic conductors (MIECs) such as  $\text{La}_{1-x}\text{Sr}_x\text{CoO}_{3-\delta}$  (LSC)<sup>9-15</sup> and  $\text{La}_{1-x}\text{Sr}_x\text{Co}_{1-y}\text{F}_y\text{O}_{3-\delta}$  (LSCF)<sup>16-20</sup> perovskite oxides have been studied widely to promote the oxygen surface exchange kinetics at intermediate temperatures.

Oxide heterostructured interfaces such as the combination of a  $(\text{La}_{0.5}\text{Sr}_{0.5})_2\text{CoO}_{4+\delta}$  ( $\text{LSC}_{214}$ ) Ruddlesden-Popper (RP) and a LSC perovskite, which can exhibit remarkably high oxygen surface exchange kinetics, have been studied intensively.<sup>21-33</sup> Sase et al.<sup>30</sup> have reported ~3 orders of magnitude higher oxygen surface exchange coefficient ( $k^*$ ) at the interfacial region between polycrystalline  $\text{La}_{0.6}\text{Sr}_{0.4}\text{CoO}_{3-\delta}$  and  $\text{LSC}_{214}$  compared to their bulk values. This enhancement has been translated to a porous composite cathode having ~1 order of magnitude enhancement in activity reported by Yashiro et al.<sup>33</sup> In addition, pronounced enhancement in the surface exchange kinetics up to ~2 orders of magnitude<sup>22</sup> has been reported by decorating epitaxially grown  $\text{LSC}_{214}$  on (001)-oriented  $\text{La}_{0.8}\text{Sr}_{0.2}\text{CoO}_{3-\delta}$  ( $\text{LSC}_{113}$ ). Recent experimental and density functional theory (DFT) studies have suggested that the enhancement can be attributed to surface segregation of Sr in the perovskite structure at the  $\text{LSC}_{214}$ - $\text{LSC}_{113}$  interface and surface segregation of Sr on the  $\text{LSC}_{214}$  surface.<sup>23-26</sup>

In this work, we focus on the influence of  $\text{LSC}_{214}$  surface decoration on the oxygen surface exchange kinetics and the time-dependent surface stability of epitaxial

$\text{La}_{0.6}\text{Sr}_{0.4}\text{Co}_{0.2}\text{Fe}_{0.8}\text{O}_{3-\delta}$  (LSCF<sub>113</sub>) thin films, which is compared with an LSC<sub>214</sub>-decorated LSC<sub>113</sub> thin film. Therefore, in this study, we address if and how LSC<sub>214</sub> decoration on the LSCF<sub>113</sub> surface can lead to any enhancement of the surface exchange kinetics and surface stability using epitaxial thin films as a model system. As part of this study, we provide DFT predictions of surface stability and composition (La/Sr and Co/Fe segregation) for LSC<sub>113</sub> and LSCF<sub>113</sub> (001) surfaces. We find that the LSC<sub>214</sub> decoration can enhance the oxygen surface exchange coefficient ( $k^{\text{q}}$ ) of the LSCF<sub>113</sub> thin film only  $\sim 2$  times in contrast to the pronounced enhancement in the  $k^{\text{q}}$  by  $\sim 2$  orders of magnitude observed for the LSC<sub>113</sub> thin film found in this study and previous work.<sup>22, 34</sup> We report that the LSC<sub>214</sub>-decorated LSC<sub>113</sub> exhibits much reduced degradation in  $k^{\text{q}}$  relative to LSC<sub>113</sub> while LSC<sub>214</sub>-decorated LSCF<sub>113</sub> and LSCF<sub>113</sub> show comparable loss in the surface exchange kinetics over time. Combined Auger electron spectroscopy (AES) and DFT studies suggest that reduced degradation associated with LSC<sub>214</sub> decoration of LSC<sub>113</sub> over time and the lack of changes associated with LSC<sub>214</sub> decoration of LSCF<sub>113</sub> can be attributed to stabilization of LSC<sub>113</sub> surface by LSC<sub>214</sub> decoration and greater stability of LSCF<sub>113</sub> against decomposition into secondary phases than LSC<sub>113</sub>.

## 2. Experimental Methods

### 2.1 Film deposition

Pulsed laser deposition (PLD) was utilized to deposit the (001)-oriented epitaxial LSCF<sub>113</sub> thin films ( $\sim 62.5$  nm) on YSZ with a  $\sim 5$  nm gadolinium-doped ceria (GDC, 20 mol % Gd) as the buffer layer to prevent the formation of  $\text{La}_2\text{Zr}_2\text{O}_7$ .<sup>35</sup> Varying thicknesses of LSC<sub>214</sub> ( $\sim 0.26$ ,  $\sim 0.78$ ,  $\sim 2.6$ , and  $\sim 5$  nm) were deposited subsequently on top of the LSCF<sub>113</sub>/GDC/YSZ.

The epitaxial LSC<sub>113</sub> thin films (~85 nm) with and without LSC<sub>214</sub> decoration (~2.6 nm) were also prepared on YSZ(001) with a GDC buffer layer using PLD. Details for the LSCF<sub>113</sub>, LSC<sub>214</sub>, LSC<sub>113</sub>, and GDC PLD target syntheses and PLD deposition process can be found in the Electronic Supplementary Information (ESI†).

## 2.2 High resolution X-ray diffraction (HRXRD)

Oxide phase purity and orientation of the thin film systems were investigated via high resolution X-ray diffraction (HRXRD) using a four-circle diffractometer (PANalytical, USA and Bruker D8, Germany). Measurements were performed in normal and off-normal configurations. The in-plane lattice parameters (*a* lattice parameter) of LSCF<sub>113</sub> and LSC<sub>113</sub> was determined from the off-normal (202)<sub>pc</sub> peak position (where “pc” denotes the pseudocubic notation) and the *c* lattice parameter of LSCF<sub>113</sub> and LSC<sub>113</sub> normal to the film surface was determined from the (002)<sub>pc</sub> peak position. Surface morphology was examined by optical microscopy (Carl Zeiss, Germany) and atomic force microscopy (AFM) (Veeco, USA). AFM images of as-deposited LSCF<sub>113</sub> and LSC<sub>214</sub>-decorated LSCF<sub>113</sub> films revealed that the surfaces were smooth with the root-mean-square (RMS) roughness values of 0.237 – 0.323 nm, as shown in Fig. S1†. Indeed, those of as-deposited LSC<sub>113</sub> and LSC<sub>214</sub>-decorated LSC<sub>113</sub> films also showed very smooth surfaces with the RMS roughness values of 0.769 – 1.133 nm, as shown in Fig. 5. The RMS roughness was comparable across all surfaces.

## 2.3 Electrochemical impedance spectroscopy (EIS)

Electrochemical impedance spectroscopy (EIS) measurements of microelectrodes ~200 μm in diameter were performed using a microprobe station (Karl Süss, Germany) connected to a

frequency response analyzer (Solartron 1260, USA) and dielectric interface (Solartron 1296, USA). Temperature was controlled at 550 °C with heating stage (Linkam TS1500, UK) and data were collected between 1 MHz to 1 mHz using a voltage amplitude of 10 mV. EIS testing temperature was calibrated with a thermocouple contacting the thin film surface and deviation of  $\pm 5$  °C was observed. EIS experiments were completed between  $p(\text{O}_2)$  of  $10^{-3}$  atm and 1 atm. EIS data were analyzed using an equivalent circuit (Fig. S4b†), from which the ORR resistance ( $R_{\text{ORR}}$ ) and surface exchange rate were obtained. Details about the EIS testing procedure, data analysis, and  $c_0$  estimation can be found in the ESI†.

## 2.4 Auger electron spectroscopy (AES)

Auger electron spectroscopy (AES) was conducted using a Physical Electronics 700 Scanning Auger Nanoprobe (PHI, USA) operating at an accelerating voltage of 10 kV to analyze the surface chemistry change of the  $\text{LSC}_{214}$ -decorated  $\text{LSCF}_{113}$  and the  $\text{LSC}_{214}$ -decorated  $\text{LSC}_{113}$  films after heat treatment. The films were annealed at 550 °C for 6 hours in an oxygen partial pressure of 1 atm before AES data were collected. The AES data were collected using two different modes: area mode (three different  $10 \mu\text{m} \times 10 \mu\text{m}$  regions selected across a sample) and point mode (two different  $\sim 0.45 \mu\text{m}$  diameter spots selected on a sample) in an ultra-high vacuum chamber. Elemental quantification of AES spectra utilized relative sensitivity factors (RSFs) of 0.059, 0.027, 0.076, 0.178, and 0.212 for  $\text{La}_{\text{MNN}}$ ,  $\text{Sr}_{\text{LMM}}$ ,  $\text{Co}_{\text{LMM}}$ ,  $\text{Fe}_{\text{LMM}}$ , and  $\text{O}_{\text{KLL}}$ , respectively, as supplied by the AES manufacturer (Physical Electronics). Details about AES measurement and analysis can be found in the ESI†.

## 2.5 Density functional theory (DFT)

Spin polarized Density Functional Theory (DFT) calculations are performed with the Vienna *Ab-initio* Simulation Package<sup>36, 37</sup> using the Projector-Augmented plane-Wave method.<sup>38</sup> Exchange-correlation is treated in the Perdew-Wang-91<sup>39</sup> Generalized Gradient Approximation (GGA). The GGA+*U* calculations<sup>40</sup> are performed with the simplified spherically averaged approach,<sup>41</sup> where the  $U_{eff}$  ( $U_{eff}$  = Coulomb  $U$  - exchange  $J$ ) is applied to  $d$  electrons. ( $U_{eff}(\text{Fe}) = 4.0$  eV and  $U_{eff}(\text{Co}) = 3.3$  eV).<sup>25, 42</sup> All calculations are performed in the ferromagnetic state in order to use a consistent and tractable set of magnetic structures.

Calculations for  $\text{Sr}_{\text{La}}$  substitution energies in bulk  $\text{LSC}_{113}$  and  $\text{LSCF}_{113}$  are simulated using a  $2a_{pv} \times 2a_{pv} \times 2a_{pv}$  pseudocubic supercell structure of  $\text{La}_{0.75}\text{Sr}_{0.25}\text{CoO}_3$  (with  $a_{pv}(\text{La}_{0.75}\text{Sr}_{0.25}\text{CoO}_3) = 3.88$  Å, where  $a_{pv}$  is the relaxed GGA+*U* perovskite lattice constant) and  $\text{La}_{0.625}\text{Sr}_{0.375}\text{Fe}_{0.75}\text{Co}_{0.25}\text{O}_3$  ( $a_{pv}(\text{LSCF}_{113}) = 3.91$  Å) with  $2 \times 2 \times 2$  k-point mesh and 450 eV plane-wave energy cut-off.  $\text{Sr}_{\text{La}}$  substitution energy in bulk  $\text{LSC}_{214}$  is simulated using a  $2a_{rp} \times 2a_{rp} \times c_{rp}$  supercell structure of  $\text{LSC}_{214}$  (where  $a_{rp}$  and  $c_{rp}$  are the relaxed GGA+*U* RP phase lattice constant:  $a_{rp}(\text{LSC}_{214}) = 3.86$  Å,  $c_{rp}(\text{LSC}_{214}) = 12.50$  Å).<sup>43</sup> The supercell configurations are illustrated in Fig. S8†. The  $\text{Sr}_{\text{La}}$  substitution energy for  $\text{La}_{0.75}\text{Sr}_{0.25}\text{CoO}_3$  ( $\text{La}_{0.625}\text{Sr}_{0.375}\text{Fe}_{0.75}\text{Co}_{0.25}\text{O}_3$ ) bulk was taken as the difference in energies between a  $\text{La}_{0.625}\text{Sr}_{0.375}\text{CoO}_3$  ( $\text{La}_{0.5}\text{Sr}_{0.5}\text{Fe}_{0.75}\text{Co}_{0.25}\text{O}_3$ ) bulk and a  $\text{La}_{0.75}\text{Sr}_{0.25}\text{CoO}_3$  ( $\text{La}_{0.625}\text{Sr}_{0.375}\text{Fe}_{0.75}\text{Co}_{0.25}\text{O}_3$ ) bulk. Similarly, the  $\text{Sr}_{\text{La}}$  substitution energy for  $\text{LSC}_{214}$  was calculated using the total energy difference between  $(\text{La}_{0.5}\text{Sr}_{0.5})_2\text{CoO}_4$  and  $(\text{La}_{0.4375}\text{Sr}_{0.5625})_2\text{CoO}_4$ .

The  $\text{LSC}_{214}$ - $\text{LSCF}_{113}$  heterointerface was simulated with a periodic 176-atom supercell ( $2a_{113} \times 2a_{113}$  supercell in the x-y plane ( $a_{113} = a_{pv}(\text{LSCF}_{113}) = 3.91$  Å) with 12-layers of  $\text{La}_{0.625}\text{Sr}_{0.375}\text{Fe}_{0.75}\text{Co}_{0.25}\text{O}_3$  and 6-layers of  $\text{LSC}_{214}$  along  $z$  where the relaxed  $c_{rp}(\text{LSC}_{214}) = 12.42$  Å). The  $\text{LSC}_{214}$ - $\text{LSCF}_{113}$  heterointerface calculations and structural model were adopted based on

those reported previously for LSC<sub>214</sub>-LSC<sub>113</sub>.<sup>24, 25</sup> Three different Sr/La and Co/Fe arrangements in the LSC<sub>214</sub>-LSCF<sub>113</sub> interface model are investigated, as shown in Fig. S8†.

*Ab initio* thermodynamic analysis for LSC<sub>113</sub> and LSCF<sub>113</sub> surface stability are simulated using the 9-layer 2×2 symmetric (001) AO terminated and BO<sub>2</sub> terminated slabs with the central 5 layers fixed to a composition close to the bulk LSC<sub>113</sub> and LSCF<sub>113</sub>. The La/Sr (and Fe/Co for LSCF<sub>113</sub>) content of the top two and bottom two layers are varied, as illustrated in Fig. S11†. LaSrCoO<sub>4</sub> surface calculations are performed using the 9-layer 2×2 symmetric (001) AO terminated and 8-layer (100) A<sub>2</sub>BO<sub>4</sub> terminated slabs with the top and bottom surface layers varying the A-site Sr concentration and the rest of the slab composition fixed to LaSrCoO<sub>4</sub>, as also illustrated in Fig. S11†. More details of the *ab initio* methods and thermodynamic analysis are provided in the ESI†.

### 3. Results and Discussion

#### 3.1 Structural relationship of epitaxial LSCF<sub>113</sub> thin films with LSC<sub>214</sub> decoration

Normal XRD data (Fig. 1) of the undecorated LSCF<sub>113</sub> and LSC<sub>214</sub>-decorated LSCF<sub>113</sub> films clearly show the presence of the (00*l*)<sub>pc</sub> (*l* is integer) peaks of LSCF<sub>113</sub> and (00*l*)<sub>cubic</sub> (*l* is even) peaks of GDC and YSZ, indicating that the LSCF<sub>113</sub> film grew epitaxially with the following epitaxial relationships: (001)<sub>pc</sub>LSCF<sub>113</sub> // (001)<sub>cubic</sub>GDC // (001)<sub>cubic</sub>YSZ. With LSC<sub>214</sub> coverage equal to ~5 nm in thickness, the (00*l*)<sub>tetra.</sub> (*l* is integer) peaks of LSC<sub>214</sub> become visible, which represents (001)<sub>tetra.</sub>LSC<sub>214</sub> // (001)<sub>pc</sub>LSCF<sub>113</sub> // (001)<sub>cubic</sub>GDC // (001)<sub>cubic</sub>YSZ. The subscript “tetra.” denotes the tetragonal notation.<sup>44, 45</sup> Off-normal phi-scan analysis of the undecorated LSCF<sub>113</sub> and LSC<sub>214</sub>-decorated LSCF<sub>113</sub> films shows that LSC<sub>214</sub> {103}<sub>tetra.</sub>, LSC<sub>113</sub>

$\{101\}_{\text{pc}}$ , GDC  $\{202\}_{\text{cubic}}$  and YSZ  $\{202\}_{\text{cubic}}$  have strong peaks with 4-fold cubic symmetry (Fig. 1b), which reveal the in-plane crystallographic relationships between GDC and YSZ (a cube-on-cube alignment), LSCF<sub>113</sub> and GDC (an in-plane 45° rotation with  $[100]_{\text{pc}}\text{LSCF}_{113} // [110]_{\text{cubic}}\text{GDC} // [110]_{\text{cubic}}\text{YSZ}$ ), and LSCF<sub>113</sub> and LSC<sub>214</sub> (no rotation with  $[100]_{\text{pc}}\text{LSCF}_{113} // [100]_{\text{tetra}}\text{LSC}_{214}$ ), as shown in Fig. 1c. The undecorated LSC<sub>113</sub> and LSC<sub>214</sub>-decorated LSC<sub>113</sub> thin films also had the same crystallographic relationships as shown in Fig. S2†. Similar to our previous studies,<sup>22, 23, 46</sup> the relaxed lattice parameters,  $\hat{a}$  of the epitaxial LSCF<sub>113</sub> films with and without LSC<sub>214</sub> surface decoration in this study at room temperature did not change significantly with different LSC<sub>214</sub> decoration thicknesses, ranging from 3.902 – 3.906 Å (Fig. S3a†). The  $\hat{a}$  of the epitaxial LSC<sub>113</sub> films with and without LSC<sub>214</sub> surface decoration was also found not to change significantly, having 3.838 – 3.839 Å (Fig. S3a†). As shown in Fig. S3b†, both in-plane and out-of-plane strains of LSCF<sub>113</sub> and LSC<sub>113</sub> films were not strongly influenced by the LSC<sub>214</sub> coverage, which is supported by the fact that the lattice constant of LSC<sub>214</sub> ( $a_{\text{tetra}} \approx 3.819$  Å for LSC<sub>214</sub> bulk<sup>47</sup>) is very close to that of LSCF<sub>113</sub> ( $a_{\text{tetra}} \approx 3.885$  Å for LSCF<sub>113</sub> bulk<sup>19</sup>) and LSC<sub>113</sub> ( $a_{\text{tetra}} \approx 3.854$  Å for LSC<sub>113</sub> bulk<sup>48</sup>). This observation is further supported by our recent work,<sup>23</sup> where the LSC<sub>214</sub> decoration has no influence on the in-plane and out-of-plane strains of the epitaxial LSC<sub>113</sub> films at elevated temperatures. Details about lattice parameter calculation and HRXRD of LSC<sub>214</sub>-decorated LSC<sub>113</sub> film can be found in the ESI†.

### **3.2 Oxygen surface exchange kinetics of the LSCF<sub>113</sub> and LSC<sub>113</sub> with and without LSC<sub>214</sub> decoration**

EIS data collected from the undecorated LSCF<sub>113</sub> and LSC<sub>214</sub>-decorated LSCF<sub>113</sub> films at 550 °C with an oxygen partial pressure of 1 atm are shown in Fig. 2a. The real impedance of the

predominant semicircle decreased slightly with LSC<sub>214</sub> coverage. In addition, the predominant semicircle was found to increase with decreasing oxygen partial pressure, where EIS data of all samples used in this study were found to show nearly perfect semicircle impedances.<sup>49</sup> Representative EIS data collected from the LSCF<sub>113</sub> film with ~5 nm LSC<sub>214</sub> coverage measured at 550 °C as a function of  $p(\text{O}_2)$  are shown in Fig. 2b. Considering the fact that the film thicknesses are much smaller than the critical thickness for bulk transport limitation (estimated to 3.28  $\mu\text{m}$  for bulk LSCF<sub>113</sub> at 550 °C<sup>50</sup>), the ORR kinetics are limited by surface oxygen exchange but not by oxygen ion diffusion. This is in agreement with the  $p(\text{O}_2)$ -dependent impedance responses, as expected for a surface exchange limited electrode.<sup>46, 51-53</sup> Similar to LSCF<sub>113</sub> thin films, LSC<sub>214</sub>-decorated LSC<sub>113</sub> thin film, where the film thicknesses are much smaller than the critical thickness (estimated to 1  $\mu\text{m}$  for bulk LSC<sub>113</sub> at 550 °C<sup>6</sup>), also showed the  $p(\text{O}_2)$ -dependent impedance responses (Fig. S5†), suggesting that the oxygen surface exchange kinetics governs the oxygen electrocatalysis on the film surface.

The  $k^q$  of the undecorated LSCF<sub>113</sub> was found to be higher than that of the undecorated LSC<sub>113</sub>, which is in good agreement with our previous experimental studies and consistent with recent trends correlated  $k^q$  with the bulk oxygen  $p$ -band center,<sup>54</sup> which is found to be higher in the LSCF<sub>113</sub> than the LSC<sub>113</sub>. It should be noted that LSC<sub>214</sub> coverage led to only 1 – 2 times enhancement of the  $k^q$  values of the undecorated LSCF<sub>113</sub> thin films while the  $k^q$  of LSC<sub>113</sub> with LSC<sub>214</sub> coverage was found to be nearly 2 orders of magnitude higher than that of the undecorated LSC<sub>113</sub>. As Han et al. have proposed that both the anisotropy of LSC<sub>214</sub> and the lattice strain near the interface between LSC<sub>214</sub> and LSC<sub>113</sub> are responsible for the significantly enhanced surface exchange kinetics of heterostructured oxide interface,<sup>26</sup> we also examined the average strains in the films. However, LSC<sub>214</sub> decoration had no detectable influence on the

average strains of either LSCF<sub>113</sub> or LSC<sub>113</sub> films, as shown in Fig. S3†, suggesting that strain was not playing a critical role in these samples.

The volume specific capacitances (*VSCs*) of the LSCF<sub>113</sub> and LSC<sub>113</sub> films, corresponding to the change in the oxygen nonstoichiometry ( $\delta$ ) induced by the change in the electrical potential, did not change significantly with LSC<sub>214</sub> surface coverage, as shown in Fig. 2d. This result is in good agreement with our previous results<sup>22</sup> where LSC<sub>214</sub> surface coverage has no influence on the oxygen vacancy concentration of LSC<sub>113</sub> thin films. Moreover, the *VSCs* of LSC<sub>113</sub> with and without LSC<sub>214</sub> decoration in this study were comparable to those of epitaxial LSC<sub>113</sub> thin films reported previously.<sup>53</sup> This result indicates that the oxygen content in the LSC<sub>113</sub> and LSCF<sub>113</sub> films with and without LSC<sub>214</sub> coverage do not contribute to the modification of the  $k^q$  values observed, suggesting that the changes in  $k^q$  values are due to changes in surface chemistry. Details of *VSCs* are provided in the ESI†.

The LSC<sub>214</sub> decoration can also greatly reduce the time-dependent degradation of the oxygen surface exchange kinetics of the LSC<sub>113</sub> thin film, as shown in Fig. 3a. After annealing at 550 °C for 70 hours, the  $k^q$  values of the undecorated LSC<sub>113</sub> was found to significantly decrease as annealing time increases, consistent with results shown by Kubicek, et al.,<sup>55</sup> while LSC<sub>214</sub>-decorated LSC<sub>113</sub> showed a relatively small reduction in the  $k^q$  values after 70 hours annealing. In contrast, LSC<sub>214</sub> decoration had no influence on preventing the time-dependent degradation of the oxygen surface exchange kinetics of the LSCF<sub>113</sub> thin film (Fig. 3b). Regardless of the LSC<sub>214</sub> decoration, the time-dependent degradation of the oxygen surface exchange kinetics of the LSCF<sub>113</sub> thin films was found to show similar reduction in the  $k^q$  values as a function of annealing time. The *VSCs* of the LSC<sub>113</sub> and LSCF<sub>113</sub> with and without LSC<sub>214</sub> coverage was found to not change significantly with increasing the annealing time (Fig. S6†), which indicates

that the degradation of the oxygen surface exchange kinetics as a function of time does not depend on the bulk oxygen content.

### **3.3 Surface chemistry and stability changes of the LSCF<sub>113</sub> and LSC<sub>113</sub> with and without LSC<sub>214</sub> decoration**

The changes in the surface chemistry of LSC<sub>113</sub> and LSCF<sub>113</sub> films without and with LSC<sub>214</sub> decoration before and after annealing at 550 °C for 6 hours were revealed by Auger electron spectroscopy (AES) using area mode (three different 10 μm × 10 μm regions selected across a sample), as shown in Fig. 4. La Auger signals of the undecorated LSC<sub>113</sub> surface were found to decrease with LSC<sub>214</sub> coverage (Fig. 4a) while Sr Auger signals were found to increase (Fig. 4b). In contrast, the changes in La and Sr Auger signals of LSCF<sub>113</sub> film surfaces with and without LSC<sub>214</sub> coverage were considerably smaller than those observed for LSC<sub>113</sub> (negligible changes noted for Sr Auger), as shown in Figs. 4c and 4d. LSC<sub>214</sub> decoration led to a greater increase in the Sr/La ratio for the LSC<sub>214</sub>-decorated LSC<sub>113</sub> surface than LSC<sub>214</sub>-decorated LSCF<sub>113</sub>, as shown in Fig. 4f. The large increase in the surface Sr/La ratio for LSC<sub>214</sub>-decorated LSC<sub>113</sub> relative to LSC<sub>113</sub> is in good agreement with our recent COBRA and DFT studies,<sup>24</sup> which reveals pronounced strontium (Sr) segregation at the interface of LSC<sub>113</sub> and LSC<sub>214</sub> and near the surface of LSC<sub>214</sub>. The surface Sr concentration of the LSC<sub>113</sub> and LSCF<sub>113</sub> modulated by LSC<sub>214</sub> coverage can be associated with a change in the oxygen 2*p* band center (relative to the Fermi level), which can contribute to the enhancement of the oxygen surface exchange kinetics. This hypothesis will be explored with DFT calculations and further discussed in section 3.6.

The LSC<sub>214</sub> decoration was found to influence the surface stability of LSC<sub>113</sub> and LSCF<sub>113</sub> at elevated temperatures. AFM imaging revealed that as-deposited LSC<sub>113</sub> with and

without LSC<sub>214</sub> coverage had nearly atomically flat surfaces with RMS roughness ~1 nm, having no discrete particles on the surfaces before annealing, as shown in Fig. 5b and 5c. After annealing at 550 °C for 6 hours, discrete particles, which have higher Sr Auger signals (Fig. S7†) than the rest of the surface as well as the surfaces before annealing, were noted on the undecorated LSC<sub>113</sub> (Fig. 5f). This observation is consistent with our recent *in situ* X-ray reflectivity (XRR) studies of surface structure and chemistry changes of LSC<sub>113</sub> films<sup>23</sup> and detection of Sr-enriched particles on the film surface from *in situ* ambient pressure X-ray photoelectron spectroscopy measurements.<sup>34, 56</sup> It has been proposed that LSC<sub>113</sub> surface decomposes to SrO-like, (La<sub>1-x</sub>Sr<sub>x</sub>)<sub>2</sub>CoO<sub>4</sub>-like, and CoO<sub>x</sub>-like phases with increasing temperature.<sup>57, 58</sup> In contrast to LSC<sub>113</sub>, no particles were found on the LSC<sub>214</sub>-decorated LSC<sub>113</sub> surface after annealing for 6 hours, which indicates that LSC<sub>214</sub> decoration can stabilize the LSC<sub>113</sub> surface, and suppress the formation of Sr-enriched particles on the LSC<sub>113</sub> surface. In contrast, no particles was found on the LSCF<sub>113</sub> surface with and without LSC<sub>214</sub> coverage after annealing at 550 °C for 6 hours (Fig. 5h and 5i), which suggests that the (001) LSCF<sub>113</sub> surface is thermodynamically more stable against decomposition than that of LSC<sub>113</sub> at elevated temperatures. The physical origins of the observed different surface stability may be attributed to the thermodynamic stability of the LSC<sub>113</sub> and LSCF<sub>113</sub> with and without LSC<sub>214</sub> coverage, which will be explored with *ab initio* DFT modeling in section 3.4.

Modulating surface chemistry by perturbing chemical potentials of elements near the surfaces region with LSC<sub>214</sub> decoration can influence the surface stability (Fig. 5) of LSC<sub>214</sub>-decorated LSC<sub>113</sub> and LSCF<sub>113</sub> films. Discrete particles, which have higher Sr Auger signals (Fig. 5a), form on the surfaces of all samples after annealing for 70 hours, as shown in Fig. 5. The chemistry of these Sr-enriched particles is not well understood. In the case of the undecorated

LSC<sub>113</sub>, however, recent COBRA experiments suggest that these Sr-enriched particles on the LSC<sub>113</sub> thin films have a composition approaching to that of SrCoO<sub>3-δ</sub>,<sup>59</sup> which is likely to coexist with or decompose to secondary phases such as SrO/Sr(OH)<sub>2</sub>/SrCO<sub>3</sub><sup>60, 61</sup> and (La,Sr)<sub>2</sub>CoO<sub>4±δ</sub>,<sup>62</sup> leading to surface passivation for the oxygen exchange kinetics.<sup>63</sup> Similar to the LSC<sub>113</sub>, LSCF<sub>113</sub> can decompose into A<sub>2</sub>BO<sub>4</sub><sup>18</sup> after annealing over 16 hours and is also susceptible to the formation of the surface Sr-enriched particles,<sup>64</sup> which contribute to degradation of cell performance.<sup>65</sup> As the Sr spectra of the particles on the LSC<sub>214</sub>-decorated LSC<sub>113</sub> was found to resemble that of an as-deposited LSC<sub>214</sub> sample prepared by PLD, it is postulated that the discrete particles on the LSC<sub>214</sub>-decorated LSC<sub>113</sub> result from agglomeration of LSC<sub>214</sub> coverage,<sup>66</sup> which reduces active heterointerface region,<sup>22</sup> and/or the decomposition of the LSC<sub>113</sub> and LSC<sub>214</sub> coverage<sup>67</sup> induced by higher Sr concentration through the cation interdiffusion for long annealing time, leading to reduction in the  $k^q$  values after 70 hours annealing for the LSC<sub>214</sub>-decorated LSC<sub>113</sub>. In the case of the LSC<sub>214</sub>-decorated LSCF<sub>113</sub>, the particles may also be attributed to decomposition of both LSCF<sub>113</sub><sup>18</sup> and LSC<sub>214</sub> or agglomeration of LSC<sub>214</sub> coverage, which can be supported by the AES Sr spectra having a similar intensity and shape as shown in the particles on the LSCF<sub>113</sub>.

The changes in the surface chemistry by LSC<sub>214</sub> coverage can also be responsible for the observed time-dependent oxygen surface exchange kinetics of the LSC<sub>214</sub>-decorated LSC<sub>113</sub> and LSCF<sub>113</sub> films, as shown in Fig. 3. The formation of surface Sr-enriched particles can lead to the reduction in the surface exchange kinetics of LSC<sub>113</sub><sup>27, 55</sup> and result from the decomposition of LSCF<sub>113</sub>.<sup>64, 68</sup> The LSC<sub>113</sub> thin film without LSC<sub>214</sub> decoration was found to show discrete particles on the surface after annealing at 550 °C for 6 hours, in which the  $k^q$  values were reduced by ~1 order of magnitude. After 70 hours, the increased number density of discrete

particles was accompanied by a reduction in  $k^q$  (~2 orders of magnitude). It is noted that no particles were observed on the surface of LSC<sub>214</sub>-decorated LSC<sub>113</sub>, where the  $k^q$  values showed negligible changes after annealing for 6 hours and relatively small degradation of the  $k^q$  values was found after 70 hours annealing. This observation suggests that LSC<sub>214</sub> coverage can retard the time-dependent degradation of the oxygen surface exchange kinetics of the LSC<sub>113</sub> thin film, suppressing the formation of the Sr-enriched secondary particles on the surface. In contrast to the LSC<sub>113</sub> thin films, LSC<sub>214</sub> decoration was found to have no influence on the time-dependent oxygen surface exchange kinetics of LSCF<sub>113</sub>, showing similar  $k^q$  values regardless of the LSC<sub>214</sub> coverage. Furthermore, LSC<sub>214</sub> decoration was also found to have no influence on suppressing the formation of the Sr-enriched particles on the surface of LSCF<sub>113</sub>. It is hypothesized that LSCF<sub>113</sub> has higher stability against decomposition than that of LSC<sub>113</sub>, and therefore LSC<sub>214</sub> cannot contribute the enhancement of the LSCF<sub>113</sub> stability, resulting in negligible  $k^q$  enhancement after 70 hours annealing. DFT modeling and thermodynamic analysis can support this hypothesis, which will be discussed in section 3.7.

It is noted that the effects of cathode polarization can also influence on the kinetics and stability of the cathode materials and their heterointerfaces, as also revealed in our previous work.<sup>34, 57</sup> In this work, we focus on investigating how differently the heterostructured interface can influence on the surface exchange kinetics and surface stability within two different model systems, while the effect of polarization on the kinetics and stability of the heterostructured interface will be further studied in a separate work.

In the following sections, we discuss *ab initio* DFT modeling and thermodynamic analysis performed to investigate LSC<sub>113</sub> and LSCF<sub>113</sub> (001) surface stability with respect to the concentration of Sr in the top surface layer, relative stability for the Sr substitution of La (Sr<sub>La</sub>) in

bulk  $\text{LSC}_{113}$ ,  $\text{LSC}_{214}$ ,  $\text{LSCF}_{113}$ , and at the  $\text{LSC}_{214}$ - $\text{LSCF}_{113}$  heterointerfaces, and assessment of surface stability against particle formation through decomposition reaction free energy of fully Sr surface substituted (*i.e.*, SrO terminated)  $\text{LSC}_{113}$ ,  $\text{LSCF}_{113}$  and  $\text{LSC}_{214}$  to form lower order binary metal oxides or to form the RP phase with  $\text{Co}_3\text{O}_4$ .

### **3.4 *ab initio* thermodynamic assessment of stable Sr content for the $\text{LSCF}_{113}$ and $\text{LSC}_{113}$ (001) surfaces and $\text{LSC}_{214}$ (001) and (100) surfaces**

To probe the physical origin of experimentally observed surface chemistry changes in Fig. 3, *ab initio* thermodynamic analysis was performed to investigate the stability of the  $\text{LSC}_{113}$  and  $\text{LSCF}_{113}$  unreconstructed (001) surfaces vs. surface termination (*i.e.*, the AO and  $\text{BO}_2$  surfaces) with varying cation content (La-Sr content for both  $\text{LSC}_{113}$  and  $\text{LSCF}_{113}$  and Fe-Co content for  $\text{LSCF}_{113}$ ), as well as stability of the  $\text{LSC}_{214}$  (001) and (100) surface terminations at varying surface layer La-Sr concentration. It is noted that the adopted DFT models in this work are limited to describe stability of the top two surface layers at varying dopant content within the perovskite phase (or within the RP phase in case of  $\text{LSC}_{214}$ ). Chemical inhomogeneity near the surfaces, including formation of Sr-enriched secondary phases on the surfaces and in extended region beneath the surface terminations<sup>69, 70</sup> is not directly addressed in the *ab initio* thermodynamic analysis performed here. While being aware of the limitation of the adopted thermodynamic model, predicted stable surface Sr content among various material systems can be useful for trend discussions in comparisons with experimental measurements.

In this work, we focus on results for  $T = 550$  °C and  $p(\text{O}_2) = 1$  atm (details of the *ab initio* methods and the thermodynamic analysis are provided in the ESI†). Within the  $\text{LSC}_{113}$  bulk stability region set by chemical potential boundaries of thermodynamic equilibrium

between the LSC<sub>113</sub> bulk and relevant lower order oxides (specifically, SrO, La<sub>2</sub>O<sub>3</sub>, Co<sub>3</sub>O<sub>4</sub>, perovskite LaCoO<sub>3</sub>, and brownmillerite SrCoO<sub>2.5</sub>), the *ab initio* thermodynamic analysis predicts that the most stable LSC<sub>113</sub> (001) surface among the investigated (001) surface configurations is the AO surface containing ~75% Sr concentration on the A site, as shown in Fig. 6a. In addition, upon further increasing  $p(\text{O}_2)$  to 50 atm (which corresponds to increase of oxygen chemical potential by 0.13 eV per O), the predicted stable (001) surface layer Sr content within stable bulk region is found to span over both the ~75% and 100% Sr concentration in the contour plot (Fig. S12b†), while decreasing  $p(\text{O}_2)$  to 0.05 atm (which corresponds to decrease of oxygen chemical potential by 0.10 eV per O) causes the predicted stable bulk region (with the (001) AO surface containing 75% Sr concentration on the A site as the stable surface) to be shifted farther away from the area in the contour plot where the (001) AO surface layer containing 100% Sr concentration is stable (red color in the contour plot), as shown in Fig. S12c†. The increasingly stable surface Sr content with increasing  $p(\text{O}_2)$  is consistent with the reported  $p(\text{O}_2)$  dependence in surface Sr enrichment of Sr-doped LaMnO<sub>3</sub> and LSCF<sub>113</sub> perovskites,<sup>64, 71</sup> and results from minimization of surface free energy in responding to relative metal chemical potential changes in the bulk perovskites upon change of oxygen chemical potential. This origin is in contrast to the previously proposed model based on point defect stability vs.  $p(\text{O}_2)$  and their interactions with the Sr dopant (attraction for oxygen vacancy and repulsion for cation vacancies) proposed by Lee et al.<sup>71</sup> and Crumlin et al..<sup>56</sup>

The surface phase diagrams of the stable (001) surface layer (including stable termination and Sr/La and Fe/Co concentrations) for the condition of effective Fe chemical potential in LSCF<sub>113</sub> equal to -0.12 eV relative to that of Fe<sub>2</sub>O<sub>3</sub> are shown in Fig. 6b and 6c for LSCF<sub>113</sub> (001). The definition of the effective Fe chemical potential is described in the ESI†, and a

complete set of surface phase diagrams at different effective Fe chemical potentials are provided in Fig. S13† ( $\Delta\mu_{\text{Fe}}^{\text{eff}}(\text{La}_{0.625}\text{Sr}_{0.375}\text{Fe}_{0.75}\text{Co}_{0.25}\text{O}_3) = 0.0 \text{ eV}, 0.0, -0.24, -0.36 \text{ eV}$  vs.  $\mu_{\text{Fe}}^{\text{eff}}(\text{Fe}_2\text{O}_3)$ ), as shown in Fig. S13a†, S13c†, and S13d†). The two independent effective metal chemical potentials are represented by  $\Delta\mu_{\text{Co}}^{\text{eff}}(\text{La}_{0.625}\text{Sr}_{0.375}\text{Fe}_{0.75}\text{Co}_{0.25}\text{O}_3)$  and  $\Delta\mu_{\text{Sr}}^{\text{eff}}(\text{La}_{0.625}\text{Sr}_{0.375}\text{Fe}_{0.75}\text{Co}_{0.25}\text{O}_3)$ , where  $\Delta\mu_{\text{Co}}^{\text{eff}}(\text{La}_{0.625}\text{Sr}_{0.375}\text{Fe}_{0.75}\text{Co}_{0.25}\text{O}_3) = \mu_{\text{Co}}^{\text{eff}}(\text{La}_{0.625}\text{Sr}_{0.375}\text{Fe}_{0.75}\text{Co}_{0.25}\text{O}_3) - \mu_{\text{Co}}^{\text{eff}}(\text{Co}_3\text{O}_4)$  and  $\Delta\mu_{\text{Sr}}^{\text{eff}}(\text{La}_{0.625}\text{Sr}_{0.375}\text{Fe}_{0.75}\text{Co}_{0.25}\text{O}_3) = \mu_{\text{Sr}}^{\text{eff}}(\text{La}_{0.625}\text{Sr}_{0.375}\text{Fe}_{0.75}\text{Co}_{0.25}\text{O}_3) - \mu_{\text{Sr}}^{\text{eff}}(\text{SrO})$ . The  $\text{La}_{0.625}\text{Sr}_{0.375}\text{Fe}_{0.75}\text{Co}_{0.25}\text{O}_3$  (001) surface stability analysis results predicts that the most stable surfaces are the AO surfaces with the surface layer A-site Sr concentration equal to 100% within the region of chemical potentials where the bulk material is stable relative to the lower order oxides (Fig. 6b). Such a conclusion holds for all the other investigated conditions of Fe chemical potentials, as shown in Fig. S13a†, S13c†, and S13d†. The predicted Sr concentrations can be combined with stability analysis to show that our predictions are consistent with the stability differences between (La,Sr)FeO<sub>3</sub> and (La,Sr)CoO<sub>3</sub> perovskites described in previous study<sup>72</sup> (for more details see section 3.7). The predicted LSCF<sub>113</sub> (001) surface stability results based on our *ab initio* thermodynamic analysis are in good agreement with a recent Low Energy Ion Scattering study on LSCF<sub>113</sub> pellets,<sup>73</sup> which reports the disappearance of the transition metal ions and increased Sr coverage on the LSCF<sub>113</sub> surfaces upon annealing in air at 600 °C and 800 °C.

Although the Sr segregation is quite robustly predicted, the results for Co/Fe segregation in LSCF<sub>113</sub> are more ambiguous (Fig. 6c and S13†). The ambiguity is due to the fact that the chemical potential of Co/Fe is only constrained to a range of values by the restriction of having stable bulk LSCF<sub>113</sub>. Within this range of values the most stable (sub)-surface layer Co/Fe concentration varies from about 0-50%, depending on the chemical potential of Co/Fe within the

stable bulk LSCF<sub>113</sub> region (Fig. S13†).

A similar surface stability analysis as described above was also performed for the LSC<sub>214</sub> surfaces (Fig. 6d), with varying A-site La/Sr content for the top surfaces. Due to the anisotropic nature of the RP phases the two surfaces, (001) and (100), were both considered. In fact, these two surface terminations have been shown to exhibit distinct surface exchange activities<sup>45, 74</sup> while various Sr doping concentration can also lead to changes in their relative surface stability.<sup>45</sup> Our *ab initio* thermodynamic analysis predicts that at  $p(\text{O}_2) = 1$  atm and  $T = 550$  °C the fully Sr enriched (001) AO surface is the most stable surface between the investigated (001) AO and (100) A<sub>2</sub>BO<sub>4</sub> surface configurations within the bulk LSC<sub>214</sub> stability region. In addition, the (100) A<sub>2</sub>BO<sub>4</sub> surfaces are predicted to be stable with fully enriched surface layer Sr at the A-sites within the (100) surface orientation. Comparatively, the surface energy of the fully Sr-enriched (100) A<sub>2</sub>BO<sub>4</sub> surface is found to be a factor of 1.2 ~ 2 greater than the surface energy of the fully Sr-enriched (001) AO surface within the stable bulk LaSrCoO<sub>4</sub> region, suggesting the greater stability of the (001) AO surface with fully enriched Sr vs. the (100) A<sub>2</sub>BO<sub>4</sub> surfaces.

Overall, our results suggests that at the experimental condition investigated in this work (i.e.,  $T = 550$  °C and  $p(\text{O}_2) = 1$  atm), both the stable LSCF<sub>113</sub> and LSC<sub>214</sub> (001) surfaces can exhibit higher Sr concentration than the LSC<sub>113</sub> (001) surfaces. The predicted stable surface Sr content among LSCF<sub>113</sub>, LSC<sub>113</sub>, and LSC<sub>214</sub>, along with the calculated *ab initio* Sr<sub>La</sub> substitution energies in bulk LSC<sub>113</sub>, LSCF<sub>113</sub>, LSC<sub>214</sub>, and their interfaces, are in accordance with the experimental trend in surface Sr Auger signals of the AES measurements shown in Fig. 4, as discussed previously in section 3.3.

### **3.5 *Ab initio* Sr<sub>La</sub> substitution energies in bulk LSC<sub>214</sub>, LSC<sub>113</sub>, LSCF<sub>113</sub>, and the LSC<sub>214</sub>-**

## decorated LSCF<sub>113</sub> heterointerfaces

To understand the physical origin of different enhancement on the surface Sr content in the LSCF<sub>113</sub> and LSC<sub>113</sub> films upon LSC<sub>214</sub> decoration, *ab initio* DFT calculations were performed to investigate energy for Sr substitution of La (Sr<sub>La</sub>) in the structures of LSC<sub>214</sub>, LSC<sub>113</sub>, and LSCF<sub>113</sub>, as shown in Fig. 7a (details of the DFT modeling approaches are provided in the ESI†). The calculated Sr<sub>La</sub> substitution energies in relaxed bulk LSC<sub>214</sub>, LSC<sub>113</sub>, and LSCF<sub>113</sub> (all relative to that of LSC<sub>113</sub>) suggest a weaker thermodynamic driving force (-0.12 eV) for Sr interdiffusion from LSCF<sub>113</sub> to LSC<sub>214</sub> than from LSC<sub>113</sub> to LSC<sub>214</sub> (-0.7 eV). This finding is supported by the AES results in Fig. 4f, where the LSC<sub>214</sub>-decorated LSCF<sub>113</sub> surface exhibits only a slight increase in the Sr/La ratio relative to LSCF<sub>113</sub> in contrast to significantly more enhanced Sr/La ratio on the surface of LSC<sub>214</sub>-decorated LSC<sub>113</sub> relative to LSC<sub>113</sub>. To further understand the interfacial effect on the Sr<sub>La</sub> substitution energies, three LSC<sub>214</sub>-LSCF<sub>113</sub> interface configurations with different Sr/La and Co/Fe arrangements were investigated (more detailed information of the interface models is provided in the ESI†), as shown in Fig. 7b. The most stable Sr<sub>La</sub> substitution was found to be in the first interface layer adjacent to the LSCF<sub>113</sub> region (the interfacial region is labeled with the gray dotted line). Moving from this interface layer with the most stable Sr<sub>La</sub> substitution toward the LSCF<sub>113</sub> and LSC<sub>214</sub> regions, the Sr<sub>La</sub> substitution energies become destabilized and gradually approach to the bulk LSCF<sub>113</sub> and LSC<sub>214</sub> values. The Sr<sub>La</sub> stability across the LSC<sub>214</sub>-LSCF<sub>113</sub> interface can depend on cation configurations and there is no clear trend for Sr segregation to the interface, as shown in Fig. 7b, which can be attributed largely to the small Sr<sub>La</sub> substitution energy gain (~0.2 eV) from bulk LSCF<sub>113</sub> to bulk LSC<sub>214</sub>. In contrast, there is a more clear energetic trend for the LSC<sub>113</sub>-LSC<sub>214</sub> interface,<sup>25</sup> where Sr<sub>La</sub> substitution becomes monotonically more stabilized moving from the LSC<sub>113</sub> toward the

LSC<sub>214</sub> region, which can be attributed to the ~1 eV difference in the relative Sr<sub>L<sub>a</sub></sub> stability between the bulk LSC<sub>113</sub> and LSC<sub>214</sub>. The energies in Fig. 7b represent thermodynamic driving forces of Sr<sub>L<sub>a</sub></sub> substitution (relative to the bulk LSC<sub>113</sub>) for the simulated configurations close to the nominal bulk phase composition, rather than the equilibrated interfacial configurations. We note that the as-grown LSCF<sub>113</sub> film surfaces may be initially Sr enriched,<sup>75</sup> and consequently the thermodynamic driving force for Sr<sub>L<sub>a</sub></sub> interdiffusion from the decorated LSC<sub>214</sub> phase back to the Sr-enriched LSC<sub>214</sub>-LSCF<sub>113</sub> interfaces is expected to be reduced as compared to the energetic results shown in Fig. 7b.

In comparison with the experimental observations, here we use the *ab initio* modeling of the thermodynamically stable LSCF<sub>113</sub>, LSC<sub>113</sub>, and LSC<sub>214</sub> surfaces, the thermodynamic driving forces for Sr<sub>L<sub>a</sub></sub> substitution in bulk LSC<sub>113</sub>, LSC<sub>214</sub>, and LSCF<sub>113</sub> as well as the LSC<sub>214</sub>-LSC<sub>113</sub> and LSC<sub>214</sub>-LSCF<sub>113</sub> heterointerfaces, to discuss possible physical origins leading to the different stability for the (001) LSC<sub>113</sub> and LSCF<sub>113</sub> surfaces with and without LSC<sub>214</sub> decoration. DFT computed thermodynamic driving forces of Sr<sub>L<sub>a</sub></sub> substitution from the LSC<sub>113</sub> to interface of LSC<sub>113</sub> and LSC<sub>214</sub>, and to the LSC<sub>214</sub> in bulk and on the surface<sup>29,30</sup> show that LSC<sub>214</sub> decorated on LSC<sub>113</sub> acts as a Sr sink, which is in agreement with the strong Sr segregation seen in these systems, from ~60% Sr at the LSC<sub>113</sub> film surfaces without the LSC<sub>214</sub> decoration to up to ~100% Sr at the LSC<sub>214</sub>-on-LSC<sub>113</sub> interface and in the LSC<sub>214</sub> bulk and on the surface.<sup>24</sup> The Sr redistribution in LSC<sub>214</sub>-on-LSC<sub>113</sub> interface films was further attributed to be responsible for the enhanced surface exchange activity, based on the upshift of the O 2*p* band centers with increasing Sr content at the interface and surface of LSC<sub>214</sub>-on-LSC<sub>113</sub>, as will be discussed below in section 3.6. In addition, the greater stability of LSC<sub>214</sub>-on-LSC<sub>113</sub> vs. LSC<sub>113</sub> with respect to surface Sr-enriched particle formation may be associated with the fact that the

(La,Sr)CoO<sub>4</sub> RP phase occurs as a La<sub>1-x</sub>Sr<sub>x</sub>CoO<sub>3-δ</sub> decomposition product or intermediate in relatively reducing environments.<sup>58, 76</sup> Considering the LSC<sub>113</sub> decomposition reaction to form LSC<sub>214</sub>, when adding more LSC<sub>214</sub> decomposition product at the LSC<sub>113</sub> surfaces may reduce the thermodynamic driving force of the LSC<sub>113</sub> decomposition reaction to form LSC<sub>214</sub> and stabilize the perovskite phase, as will also be discussed in section 3.7. Therefore, surface decoration with the LSC<sub>214</sub> phase may suppress the precipitation of the secondary particles on the LSC<sub>113</sub> surface resulting in stabilizing the perovskite phase. Similar observation of disappearance of Sr-enriched secondary phase formation on surfaces of La<sub>0.6</sub>Sr<sub>0.4</sub>CoO<sub>3-δ</sub> films with (La,Sr)CoO<sub>4</sub> powders was also reported by Unemoto et al.<sup>31</sup> In contrast, the computed DFT of Sr<sub>La</sub> substitution energies from the LSCF<sub>113</sub> to interface of LSCF<sub>113</sub> and LSC<sub>214</sub> are closer than those of LSC<sub>113</sub> vs. LSC<sub>214</sub>, and the stable LSCF<sub>113</sub> (001) surface is predicted to fully Sr enriched. Therefore, the comparable Sr<sub>La</sub> stability between LSCF<sub>113</sub> and LSC<sub>214</sub> results in weaker thermodynamic driving force on modifying the surface chemistry (Sr content) of LSCF<sub>113</sub> upon LSC<sub>214</sub> decoration. In addition, as will be shown in section 3.7, the DFT computed formation energies (relative to the binary metal oxides) of the LSCF<sub>113</sub> and the LSC<sub>214</sub> at full Sr substitution also suggest that both exhibit comparable stability against decomposition, consistent with the amount of surface particle formation upon annealing with time for LSCF<sub>113</sub> without and with LSC<sub>214</sub> decoration (Fig. 5).

### **3.6 Electronic structure changes of the LSCF<sub>113</sub> and LSC<sub>113</sub> with and without LSC<sub>214</sub> decoration**

The large and small surface exchange kinetics enhancement observed for LSC<sub>214</sub> decoration on LSC<sub>113</sub> and LSCF<sub>113</sub> film can be attributed to large and small upshift of the oxygen 2*p* band center relative to the Fermi level, respectively. Increasing Sr concentration on the A-site

in the perovskite phases has been shown to lead to upshift of the oxygen  $2p$  band center relative to the Fermi level<sup>54, 77</sup>, which correlates with the increased surface oxygen exchange kinetics. In addition, our previous work<sup>24</sup> has proposed that the upshift of the oxygen  $2p$  band centers with pronounced Sr segregation can correlate with the observed activity enhancement for oxygen surface exchange of the LSC<sub>214</sub>-decorated LSC<sub>113</sub> relative to LSC<sub>113</sub>.

We here compare the relative change of the surface exchange coefficient ( $k^q$ ) vs. the calculated O  $2p$  band centers (relative to the Fermi level) between the LSC<sub>214</sub>-decorated LSCF<sub>113</sub> (LSC<sub>113</sub>) and the LSCF<sub>113</sub> (LSC<sub>113</sub>) surfaces, as shown in Fig. 8a. We assign compositions utilizing the surface Sr content of the stable LSC<sub>113</sub> and LSCF<sub>113</sub> (001) surfaces as well as the thermodynamic driving force of Sr<sub>La</sub> substitution between LSC<sub>214</sub> vs. LSC<sub>113</sub> and LSC<sub>214</sub> vs. LSCF<sub>113</sub>. The calculated bulk O  $2p$  band centers (relative to the Fermi level) of La<sub>1-x</sub>Sr<sub>x</sub>CoO<sub>3</sub> and (La<sub>1-x</sub>Sr<sub>x</sub>)<sub>2</sub>CoO<sub>4</sub> vs. the Sr concentration,  $x$ , are provided in the inset plot of Fig. 8a, which indicates uplift of the O  $2p$  band centers (relative to the Fermi level) with increasing Sr. Based on the assumption that perovskite bulk O  $2p$  band centers can correlate with the surface defect and adsorption energetics as well as oxygen surface exchange activities,<sup>54</sup> an approximation was made to correlate the calculated bulk O  $2p$  centers calculated at assigned Sr content with the measured oxygen surface exchange activities. The LSC<sub>214</sub> decoration on LSC<sub>113</sub> leads to a highly Sr enriched top surface layer of LSC<sub>214</sub> and LSC<sub>113</sub> film<sup>24</sup> both with a higher O  $2p$  band center than the LSC<sub>113</sub> surface with lower Sr segregation (we use 62.5% Sr on the A site based on the COBRA measurement of LSC<sub>113</sub> surface layer Sr concentration<sup>75</sup>). These higher  $2p$  band centers lead to higher activities (~2 orders magnitude enhancement in  $k^q$  values). In contrast to the LSC<sub>113</sub>, the stable LSCF<sub>113</sub> (001) surface is expected to have ~100% Sr from the DFT surface thermodynamic modeling, and negligible thermodynamic driving force for Sr<sub>La</sub> interdiffusion

from the LSCF<sub>113</sub> to the LSC<sub>214</sub> (Fig. 7). Consequently, there was no significant change on the O 2*p* band centers relative to the Fermi level with LSC<sub>214</sub> decoration on LSCF<sub>113</sub>, which is in agreement with the observed 2 fold enhancement of the  $k^q$  values of LSCF<sub>113</sub>. Therefore, the distinct Sr occupancy changes within the LSC<sub>214</sub>-on-LSCF<sub>113</sub> and LSC<sub>214</sub>-on-LSC<sub>113</sub> heterostructures may be responsible for the observed enhanced surface exchange kinetics relative to the undecorated LSCF<sub>113</sub> and LSC<sub>113</sub> base films.

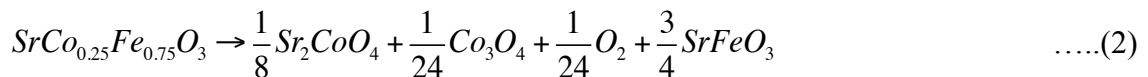
### **3.7 Stability of the LSCF<sub>113</sub>, LSC<sub>113</sub>, and LSC<sub>214</sub> at full Sr substitution relative to decomposition**

Previous COBRA studies<sup>75</sup> reveal that the top surface layer in the perovskite phase of LSC<sub>113</sub> films may contain Sr concentration at 60% on the A site and detect that discrete particles epitaxially grown to the film surface can have SrCoO<sub>3-δ</sub>-like composition, in which particle surface might be covered by electrochemically inactive Sr-rich phases (such as SrO). It was hypothesized that the surface particles of SrCoO<sub>3-δ</sub> are most likely to decompose to form secondary phases such as SrO/Sr(OH)<sub>2</sub>/SrCO<sub>3</sub>, which can greatly impede the surface exchange kinetics.<sup>63, 78</sup>

In analogy to the valence stability assessment of SOFC perovskites proposed by Yokokawa et al.,<sup>72</sup> in this section we evaluate stability of LSCF<sub>113</sub> and LSC<sub>113</sub> surfaces without vs. with LSC<sub>214</sub> decoration against surface degradation by investigating decomposition of fully Sr substituted LSCF<sub>113</sub>, LSC<sub>113</sub>, and LSC<sub>214</sub> relative to the lower order binary oxides - SrO, Co<sub>3</sub>O<sub>4</sub>, Fe<sub>2</sub>O<sub>3</sub>, based on the surface Sr content reported in the COBRA measurements,<sup>24, 59</sup> and the reported surface chemical inhomogeneity, i.e. formation of SrO like particles.<sup>55, 64</sup> Although these reaction energies are calculated for bulk compositions, we will assume the give at least

qualitative guidance for the stability of the Sr enriched surface layers. As shown in Fig. 9a, the decomposition reaction free energy to form the lower order binary metal oxides - SrO, Co<sub>3</sub>O<sub>4</sub>, Fe<sub>2</sub>O<sub>3</sub>, which is equivalent to the negative formation free energy of LSCF<sub>113</sub>, LSC<sub>113</sub>, and LSC<sub>214</sub> from the lower order binary metal oxides, are +0.443, +0.096, and +0.481 eV per formula unit at T = 550 °C and p(O<sub>2</sub>) = 1 atm, respectively. These values depend on the effective chemical potential of oxygen (see ESI† for more details of the definition on the effective chemical potential of oxygen for incorporation of temperature and p(O<sub>2</sub>) dependences in reaction free energies) and the computed *ab initio* formation energy of SrCo<sub>0.25</sub>Fe<sub>0.75</sub>O<sub>3</sub>, SrCoO<sub>3</sub>, and Sr<sub>2</sub>CoO<sub>4</sub> (Table S1†). The positive reaction free energy means that an energy penalty is required to decompose the compound, and a larger value corresponds to a higher energy cost for the decomposition reaction and higher stability of the compound. Our *ab initio* decomposition reaction free energy results suggest that SrCoO<sub>3</sub> is more prone to decompose with respect to the lower order binary metal oxides than SrCo<sub>0.25</sub>Fe<sub>0.75</sub>O<sub>3</sub> and Sr<sub>2</sub>CoO<sub>4</sub>, while both SrCo<sub>0.25</sub>Fe<sub>0.75</sub>O<sub>3</sub> and Sr<sub>2</sub>CoO<sub>4</sub> exhibit comparable stability against the decomposition at T = 550 °C and p(O<sub>2</sub>) = 1 atm.

In addition to the decomposition reaction relative to the binary metal oxides, it is also likely that decomposition of the perovskite may occur via the following reaction:<sup>58, 76, 79</sup>



As shown in Fig. 9b, the calculated reaction free energies for the reaction (1) and (2) are -0.144

eV, and -0.019 eV (or +0.011 eV with the B-site configuration entropy term for  $\text{SrCo}_{0.25}\text{Fe}_{0.75}\text{O}_3$ ), respectively, at  $T = 550\text{ }^\circ\text{C}$  and  $p(\text{O}_2) = 1\text{ atm}$ . Again, the decomposition with respect to  $\text{Sr}_2\text{CoO}_4$  and  $\text{Co}_3\text{O}_4$  formation is more exothermic for  $\text{SrCoO}_3$  than  $\text{SrCo}_{0.25}\text{Fe}_{0.75}\text{O}_3$ , indicating a poorer stability of  $\text{SrCoO}_3$  than  $\text{SrCo}_{0.25}\text{Fe}_{0.75}\text{O}_3$  with respect to formation of  $\text{Sr}_2\text{CoO}_4$  and  $\text{Co}_3\text{O}_4$ . It is also hypothesized that the  $\text{Co}_3\text{O}_4$  formation in the reaction (1) and (2) may cause degradation of surface exchange activity, due to loss of the more active perovskite phase. Therefore, upon  $\text{LSC}_{214}$  decoration, both the reaction (1) and (2) will reduce the tendency to decompose (increasing activity of the reaction product can reduce the reaction driving force), while a much weaker reduction in the thermodynamic driving force is expected for  $\text{SrCo}_{0.25}\text{Fe}_{0.75}\text{O}_3$  than  $\text{SrCoO}_3$ , as the decomposition reaction free energy of reaction (2) is close to 0 eV.

In general, these results suggest, for the high Sr content we studied, that addition of Fe stabilizes the  $\text{LSC}_{113}$  phase and that the RP structures are more stable than the  $\text{ABO}_3$  structures, at least for Co. Overall, the predicted stability trends of bulk  $\text{SrCo}_{0.25}\text{Fe}_{0.75}\text{O}_3$ ,  $\text{SrCoO}_3$ , and  $\text{Sr}_2\text{CoO}_4$  are in good agreement with the observed experimental trends of surface stability for  $\text{LSCF}_{113}$ ,  $\text{LSC}_{113}$  with and without  $\text{LSC}_{214}$  decoration, suggesting a correlation between surface degradation/particle formation and stability differences among  $\text{LSCF}_{113}$ ,  $\text{LSC}_{113}$ , and  $\text{LSC}_{214}$  against decomposition.

## 4. Conclusions

We show that  $\text{LSC}_{214}$  decoration on the (001)-oriented  $\text{LSCF}_{113}$  thin films does not greatly enhance the surface oxygen exchange kinetics in contrast to the heterostructured  $\text{LSC}_{214}$ - $\text{LSC}_{113}$  surfaces, which has surface exchange coefficients up to  $\sim 2$  orders of magnitude greater than  $\text{LSC}_{113}$ . In addition, the time-dependent degradation of the oxygen surface exchange

kinetics of the  $\text{LSC}_{113}$  thin film is markedly improved by  $\text{LSC}_{214}$  decoration in contrast to the  $\text{LSCF}_{113}$  with  $\text{LSC}_{214}$  coverage, where negligible changes are noted. AES reveals that the surface Sr concentration of the  $\text{LSC}_{113}$  significantly increases with  $\text{LSC}_{214}$  coverage, which is coupled with the suppression of the formation of secondary passive phases during annealing. In contrast,  $\text{LSC}_{214}$  decoration does not increase the surface Sr concentration of the  $\text{LSCF}_{113}$ . It is hypothesized that  $\text{LSC}_{214}$  decoration may be responsible for observed oxygen surface exchange kinetics and time-dependent surface stability, which is in good agreement with the findings from DFT studies on the thermodynamic driving force for Sr migration from the  $\text{LSCF}_{113}$  to  $\text{LSC}_{214}$  structure. *Ab initio* surface stability analysis shows that negligible increase in Sr concentration at the  $\text{LSCF}_{113}$  (001) surface perovskite surfaces can be induced by  $\text{LSC}_{214}$  decoration as the AO-terminated surface has 100% SrO and there is little driving force for Sr to segregate to the  $\text{LSCF}_{113}$  and  $\text{LSC}_{214}$  interface or into the  $\text{LSC}_{214}$  from the  $\text{LSCF}_{113}$ . However, for the  $\text{LSC}_{113}$  (001) surface there is an opportunity for significant Sr enrichment, both because the  $\text{LSC}_{113}$  (001) surface has an unsaturated A-site Sr occupation and because there is a strong driving force for Sr to migrate from  $\text{LSC}_{113}$  to the interface with  $\text{LSC}_{214}$  and into the  $\text{LSC}_{214}$  phase itself. In addition, the calculated bulk decomposition reaction free energies of  $\text{SrCo}_{0.25}\text{Fe}_{0.75}\text{O}_3$ ,  $\text{SrCoO}_3$ , and  $\text{Sr}_2\text{CoO}_4$  with respect to the binary metal oxides or formation of the  $\text{Sr}_2\text{CoO}_4$  and  $\text{Co}_3\text{O}_4$  phases correlates with the observed experimental trend of surface stability  $\text{LSCF}_{113}$ ,  $\text{LSC}_{113}$  with and without  $\text{LSC}_{214}$  decoration. This work shows that the influence of heterostructured interfaces on the oxygen surface exchange kinetics are highly dependent on the perovskite surface and surface stability, and detailed understanding on the interfacial chemistry is needed in order to use heterostructured interfaces to develop highly active and stable catalysts for oxygen electrocatalysis at elevated temperatures.

## **Associated Content**

Electronic Supplementary Information (ESI†). Details about sample preparation, EIS testing, XRD, AFM, AES, and DFT. This material is available free of charge via the Internet

## **Acknowledgements**

This work was supported by the Department of Energy (DOE), National Energy Technology Laboratory (NETL), Solid State Energy Conversion Alliance (SECA) Core Technology Program (Funding Opportunity Number DEFE0009435) and the Skoltech-MIT Center for Electrochemical Energy. The PLD and XRD performed were conducted at the Center for Nanophase Materials Sciences, which is sponsored at Oak Ridge National Laboratory by the Scientific User Facilities Division, Office of Basic Energy Sciences, U.S. Department of Energy, and computations in this work were also benefited from the use of the National Energy Research Scientific Computing Center allocation of the Center for Nanophase Materials Sciences at Oak Ridge National Laboratory, both under grant number CNMS2013-292.

## **Author Information**

Corresponding Author:

\* To whom correspondence should be addressed. [ddmorgan@wisc.edu](mailto:ddmorgan@wisc.edu), [shaohorn@mit.edu](mailto:shaohorn@mit.edu)

Author Contributions:

<sup>+</sup> These authors contributed equally to this work.

## References

1. Z. P. Shao and S. M. Haile, *Nature*, 2004, **431**, 170-173.
2. B. C. H. Steele and A. Heinzl, *Nature*, 2001, **414**, 345-352.
3. L. Yang, C. D. Zuo, S. Z. Wang, Z. Cheng and M. L. Liu, *Adv. Mater.*, 2008, **20**, 3280-3283.
4. L. da Conceicao, C. R. B. Silva, N. F. P. Ribeiro and M. Souza, *Mater. Charact.*, 2009, **60**, 1417-1423.
5. R. A. De Souza and J. A. Kilner, *Solid State Ion.*, 1998, **106**, 175-187.
6. R. A. De Souza and J. A. Kilner, *Solid State Ion.*, 1999, **126**, 153-161.
7. A. Endo, M. Ihara, H. Komiyama and K. Yamada, *Solid State Ion.*, 1996, **86-8**, 1191-1195.
8. T. Ioroi, T. Hara, Y. Uchimoto, Z. Ogumi and Z. Takehara, *J. Electrochem. Soc.*, 1997, **144**, 1362-1370.
9. S. B. Adler, *Solid State Ion.*, 1998, **111**, 125-134.
10. A. V. Berenov, A. Atkinson, J. A. Kilner, E. Bucher and W. Sitte, *Solid State Ion.*, 2010, **181**, 819-826.
11. T. Kawada, J. Suzuki, M. Sase, A. Kaimai, K. Yashiro, Y. Nigara, J. Mizusaki, K. Kawamura and H. Yugami, *J. Electrochem. Soc.*, 2002, **149**, E252-E259.
12. J. A. Kilner, R. A. DeSouza and I. C. Fullarton, *Solid State Ion.*, 1996, **86-8**, 703-709.
13. J. Mizusaki, Y. Mima, S. Yamauchi, K. Fueki and H. Tagawa, *Journal of Solid State Chemistry*, 1989, **80**, 102-111.

14. V. G. Sathe, A. V. Pimpale, V. Siruguri and S. K. Paranjpe, *Journal of Physics-Condensed Matter*, 1996, **8**, 3889-3896.
15. R. H. E. vanDoorn, I. C. Fullarton, R. A. deSouza, J. A. Kilner, H. J. M. Bouwmeester and A. J. Burggraaf, *Solid State Ion.*, 1997, **96**, 1-7.
16. J. M. Bae and B. C. H. Steele, *Solid State Ion.*, 1998, **106**, 247-253.
17. A. Esquirol, N. P. Brandon, J. A. Kilner and M. Mogensen, *J. Electrochem. Soc.*, 2004, **151**, A1847-A1855.
18. S. Hashimoto, Y. Fukuda, M. Kuhn, K. Sato, K. Yashiro and J. Mizusaki, *Solid State Ion.*, 2010, **181**, 1713-1719.
19. L. W. Tai, M. M. Nasrallah, H. U. Anderson, D. M. Sparlin and S. R. Sehlin, *Solid State Ion.*, 1995, **76**, 259-271.
20. L. W. Tai, M. M. Nasrallah, H. U. Anderson, D. M. Sparlin and S. R. Sehlin, *Solid State Ion.*, 1995, **76**, 273-283.
21. Y. Chen, Cai, Z., Kuru, Y., Ma, W., Tuller, H. L. and Yildiz, B., *Adv. Energy Mater.*, 2013, **3**, 1221–1229.
22. E. J. Crumlin, E. Mutoro, S. J. Ahn, G. J. la O, D. N. Leonard, A. Borisevich, M. D. Biegalski, H. M. Christen and Y. Shao-Horn, *J. Phys. Chem. Lett.*, 2010, **1**, 3149-3155.
23. Z. Feng, E. J. Crumlin, W. T. Hong, D. Lee, E. Mutoro, M. D. Biegalski, H. Zhou, H. Bluhm, H. M. Christen and Y. Shao-Horn, *J. Phys. Chem. Lett.*, 2013, **4**, 1512-1518.
24. Z. X. Feng, Y. Yacoby, M. J. Gadre, Y. L. Lee, W. T. Hong, H. Zhou, M. D. Biegalski, H. M. Christen, S. B. Adler, D. Morgan and Y. Shao-Horn, *J. Phys. Chem. Lett.*, 2014, **5**, 1027-1034.
25. M. J. Gadre, Y. L. Lee and D. Morgan, *Physical chemistry chemical physics : PCCP*,

- 2012, **14**, 2606-2616.
26. J. W. Han and B. Yildiz, *Energy Environ. Sci.*, 2012, **5**, 8598-8607.
  27. D. Lee, Y.-L. Lee, A. Grimaud, W. T. Hong, M. D. Biegalski, D. Morgan and Y. Shao-Horn, *J. Phys. Chem. C*, 2014, **118**, 14326-14334.
  28. M. Sase, F. Hermes, T. Nakamura, K. Yashiro, K. Sato, J. Mizusaki, T. Kawada, N. Sakai, K. Yamaji, T. Horita and H. Yokokawa, in *Solid Oxide Fuel Cells 10*, eds. K. Eguchi, S. C. Singhai, H. Yokokawa and H. Mizusaki, Electrochemical Society Inc, Pennington, 2007, vol. 7, pp. 1055-1060.
  29. M. Sase, F. Hermes, K. Yashiro, K. Sato, J. Mizusaki, T. Kawada, N. Sakai and H. Yokokawa, *J. Electrochem. Soc.*, 2008, **155**, B793-B797.
  30. M. Sase, K. Yashiro, K. Sato, J. Mizusaki, T. Kawada, N. Sakai, K. Yamaji, T. Horita and H. Yokokawa, *Solid State Ion.*, 2008, **178**, 1843-1852.
  31. A. Unemoto, K. Nagao, T. Tairako, K. Amezawa and T. Kawada, in *Ionic and Mixed Conducting Ceramics 7*, eds. M. Mogensen, T. Armstrong, T. M. Gur and H. Yokokawa, Electrochemical Soc Inc, Pennington, 2010, vol. 28, pp. 59-70.
  32. K. Yashiro, T. Nakamura, M. Sase, F. Hermes, K. Sato, T. Kawada and J. Mizusaki, in *Solid Oxide Fuel Cells 10*, eds. K. Eguchi, S. C. Singhai, H. Yokokawa and H. Mizusaki, Electrochemical Society Inc, Pennington, 2007, vol. 7, pp. 1287-1292.
  33. K. Yashiro, T. Nakamura, M. Sase, F. Hermes, K. Sato, T. Kawada and J. Mizusaki, *Electrochem. Solid State Lett.*, 2009, **12**, B135-B137.
  34. E. J. Crumlin, E. Mutoro, W. T. Hong, M. D. Biegalski, H. M. Christen, Z. Liu, H. Bluhm and Y. Shao-Horn, *J. Phys. Chem. C*, 2013, **117**, 16087-16094.
  35. A. Mitterdorfer and L. J. Gauckler, *Solid State Ion.*, 1998, **111**, 185-218.

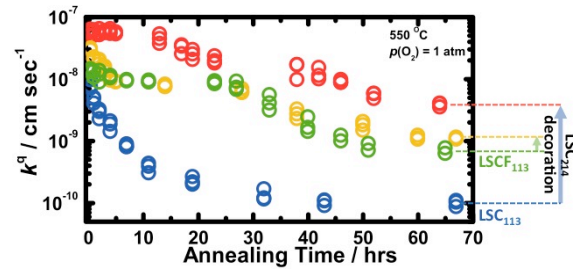
36. G. Kresse and J. Hafner, *Physical Review B*, 1993, **47**, 558.
37. G. Kresse and J. Furthmuller, *Phys. Rev. B*, 1996, **54**, 11169-11186.
38. P. E. Blochl, *Phys. Rev. B*, 1994, **50**, 17953-17979.
39. J. P. Perdew and Y. Wang, *Physical Review B*, 1992, **45**, 13244.
40. V. I. Anisimov, F. Aryasetiawan and A. I. Lichtenstein, *Journal of Physics-Condensed Matter*, 1997, **9**, 767-808.
41. S. L. Dudarev, G. A. Botton, S. Y. Savrasov, C. J. Humphreys and A. P. Sutton, *Phys. Rev. B*, 1998, **57**, 1505-1509.
42. Y.-L. Lee, J. Kleis, J. Rossmeisl and D. Morgan, *Physical Review B (Condensed Matter and Materials Physics)*, 2009, **80**, 224101.
43. C. Tealdi, C. Ferrara, L. Malavasi, P. Mustarelli, C. Ritter, G. Chiodelli and Y. A. Diaz-Fernandez, *Phys. Rev. B*, 2010, **82**, 8.
44. D. Lee, A. Grimaud, E. J. Crumlin, K. Mezghani, M. A. Habib, Z. X. Feng, W. T. Hong, M. D. Biegalski, H. M. Christen and Y. Shao-Horn, *J. Phys. Chem. C*, 2013, **117**, 18789-18795.
45. D. Lee, Y.-L. Lee, A. Grimaud, W. T. Hong, M. D. Biegalski, D. Morgan and Y. Shao-Horn, *J. Mater. Chem. A*, 2014, **2**, 6480-6487.
46. E. J. Crumlin, S. J. Ahn, D. Lee, E. Mutoro, M. D. Biegalski, H. M. Christen and Y. Shao-Horn, *J. Electrochem. Soc.*, 2012, **159**, F219-F225.
47. M. James, A. Tedesco, D. Cassidy, M. Colella and P. J. Smythe, *J. Alloy. Compd.*, 2006, **419**, 201-207.
48. R. H. E. van Doorn and A. J. Burggraaf, *Solid State Ion.*, 2000, **128**, 65-78.
49. S. B. Adler, *Chem. Rev.*, 2004, **104**, 4791-4843.

50. B. C. H. Steele and J. M. Bae, *Solid State Ion.*, 1998, **106**, 255-261.
51. F. S. Baumann, J. Fleig, H. U. Habermeier and J. Maier, *Solid State Ion.*, 2006, **177**, 1071-1081.
52. C. R. Kreller, T. J. McDonald, S. B. Adler, E. J. Crumlin, E. Mutoro, S. J. Ahn, G. J. la O, Y. Shao-Horn, M. D. Biegalski, H. M. Christen, R. R. Chater and J. A. Kilner, *J. Electrochem. Soc.*, 2013, **160**, F931-F942.
53. G. J. la O, S. J. Ahn, E. Crumlin, Y. Orikasa, M. D. Biegalski, H. M. Christen and Y. Shao-Horn, *Angew. Chem.-Int. Edit.*, 2010, **49**, 5344-5347.
54. Y. L. Lee, J. Kleis, J. Rossmeisl, Y. Shao-Horn and D. Morgan, *Energy Environ. Sci.*, 2011, **4**, 3966-3970.
55. M. Kubicek, A. Limbeck, T. Fromling, H. Hutter and J. Fleig, *J. Electrochem. Soc.*, 2011, **158**, B727-B734.
56. E. J. Crumlin, E. Mutoro, Z. Liu, M. E. Grass, M. D. Biegalski, Y. L. Lee, D. Morgan, H. M. Christen, H. Bluhm and Y. Shao-Horn, *Energy Environ. Sci.*, 2012, **5**, 6081-6088.
57. E. Mutoro, E. J. Crumlin, H. Pöpke, B. Luerssen, M. Amati, M. K. Abyaneh, M. D. Biegalski, H. M. Christen, L. Gregoratti, J. Janek and Y. Shao-Horn, *The Journal of Physical Chemistry Letters*, 2011, **3**, 40-44.
58. J. Ovenstone, J. S. White and S. T. Misture, *J. Power Sources*, 2008, **181**, 56-61.
59. Z. Feng, Y. Yacoby, W. T. Hong, H. Zhou, M. D. Biegalski, H. M. Christen and Y. Shao-Horn, *Energy Environ. Sci.*, 2014, **7**, 1166-1174.
60. H. M. Reichenbach and P. J. McGinn, *Appl. Catal. A-Gen.*, 2003, **244**, 101-114.
61. L. Karvonen, S. H. Yoon, P. Hug, H. Yamauchi, A. Weidenkaff and M. Karppinen, *Mater. Res. Bull.*, 2011, **46**, 1340-1345.

62. A. N. Petrov, V. A. Cherepanov, O. F. Kononchuk and L. Y. Gavrilova, *J. Solid State Chem.*, 1990, **87**, 69-76.
63. E. Fischer, W. D. Shen and J. L. Hertz, *J. Electroceram.*, 2012, **29**, 262-269.
64. D. Oh, D. Gostovic and E. D. Wachsman, *J. Mater. Res.*, 2012, **27**, 1992-1999.
65. Z. H. Cai, M. Kubicek, J. Fleig and B. Yildiz, *Chem. Mat.*, 2012, **24**, 1116-1127.
66. H. Huhtinen, J. Järvinen, R. Laiho, P. Paturi and J. Raittila, *Journal of Applied Physics*, 2001, **90**, 1521-1528.
67. T. Nitadori, M. Muramatsu and M. Misono, *Chem. Mat.*, 1989, **1**, 215-220.
68. H. P. Ding, A. V. Virkar, M. L. Liu and F. Liu, *Phys. Chem. Chem. Phys.*, 2013, **15**, 489-496.
69. J. Druce, H. Tellez, M. Burriel, M. D. Sharp, L. J. Fawcett, S. N. Cook, D. S. McPhail, T. Ishihara, H. H. Brongersma and J. A. Kilner, *Energy Environ. Sci.*, 2014.
70. K. Szot and W. Speier, *Phys. Rev. B*, 1999, **60**, 5909-5926.
71. W. Lee, J. W. Han, Y. Chen, Z. H. Cai and B. Yildiz, *Journal of the American Chemical Society*, 2013, **135**, 7909-7925.
72. H. Yokokawa, N. Sakai, T. Horita, K. Yamaji, M. E. Brito and H. Kishimoto, *J. Alloy. Compd.*, 2008, **452**, 41-47.
73. J. Druce, T. Ishihara and J. Kilner, *Solid State Ionics*.
74. M. Burriel, G. Garcia, J. Santiso, J. A. Kilner, J. C. C. Richard and S. J. Skinner, *J. Mater. Chem.*, 2008, **18**, 416-422.
75. Z. Feng, Y. Yacoby, W. Hong, H. Zhou, M. Biegalski, H. Christen and Y. Shao-Horn, *Energy & Environmental Science*, 2014.
76. J. Hayd, H. Yokokawa and E. Ivers-Tiffée, *J. Electrochem. Soc.*, 2013, **160**, F351-F359.

77. A. Grimaud, K. J. May, C. E. Carlton, Y. L. Lee, M. Risch, W. T. Hong, J. Zhou and Y. Shao-Horn, *Nature Communication*, 2013, **4**, 2439.
78. V. V. Vashook, M. V. Zinkevich, H. Ullmann, J. Paulsen, N. Trofimenko and K. Teske, *Solid State Ion.*, 1997, **99**, 23-32.
79. F. Morin, G. Trudel and Y. Denos, *Solid State Ion.*, 1997, **96**, 129-139.

Table of Content (max: 3.14" x 1.57")



The effect of  $(\text{La}_{0.5}\text{Sr}_{0.5})\text{CoO}_{4\pm\delta}$  decoration on the time-dependent surface exchange coefficient ( $k^q$ ) of the epitaxial  $\text{La}_{0.8}\text{Sr}_{0.2}\text{CoO}_{3-\delta}$  and  $\text{La}_{0.6}\text{Sr}_{0.4}\text{Co}_{0.2}\text{Fe}_{0.8}\text{O}_{3-\delta}$  thin films.

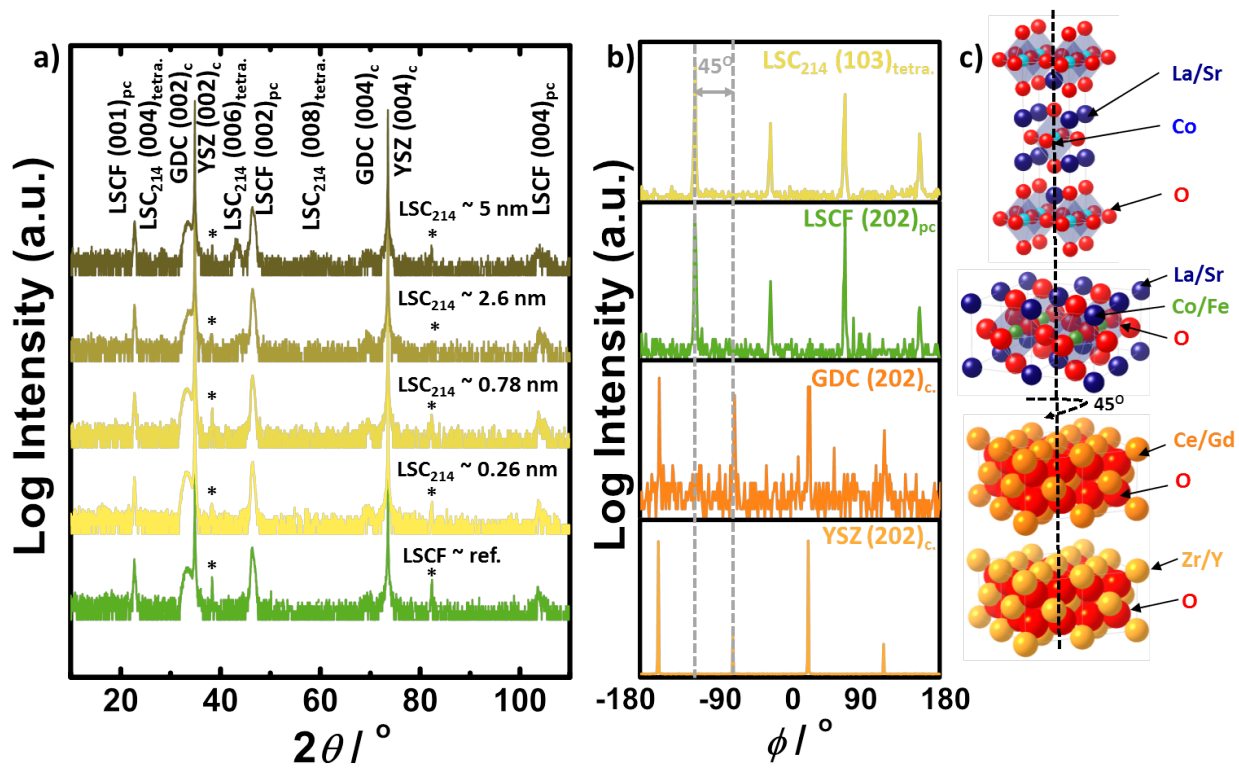


Fig. 1. X-ray diffraction (Cu  $K_\alpha$ ) analysis at room temperature. (a) Normal XRD of the epitaxial LSCF<sub>113</sub> reference and the LSC<sub>214</sub>-decorated LSCF<sub>113</sub> films, (b) off-normal XRD of a similarly prepared sample with a thicker (~5 nm) LSC<sub>214</sub> coverage, and (c) schematic of the crystallographic rotational relationships among the LSC<sub>214</sub>(001)<sub>tetra.</sub>, LSCF<sub>113</sub>(001)<sub>pc</sub>, GDC(001)<sub>cubic</sub>, and YSZ(001)<sub>cubic</sub>.

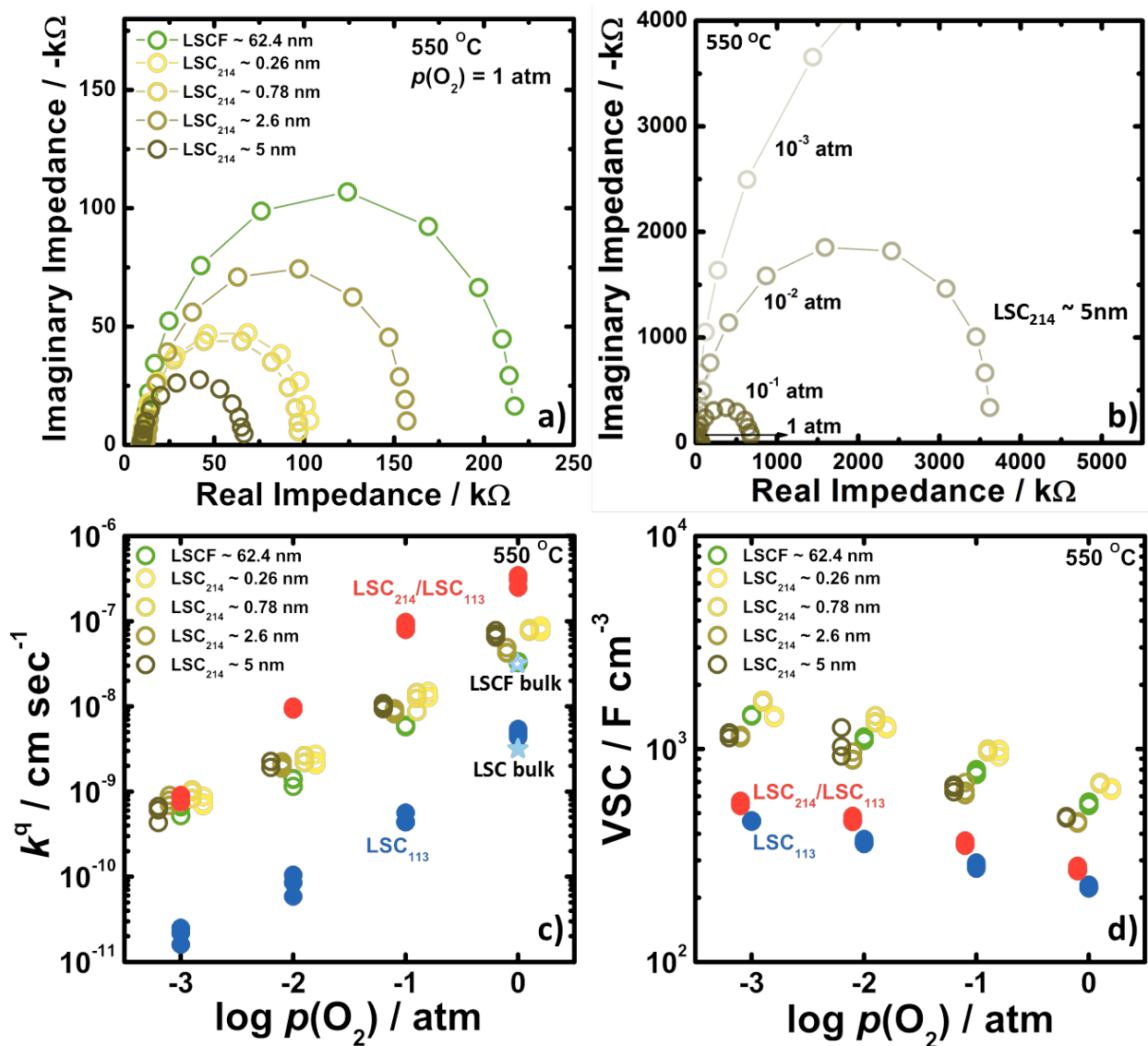


Fig. 2. Electrochemical impedance spectroscopy (EIS) results of microelectrodes ( $\sim 200 \mu\text{m}$ ) for the bare LSCF<sub>113</sub> film, LSC<sub>113</sub> film, LSCF<sub>113</sub> films with  $\sim 0.3$ ,  $\sim 0.8$ ,  $\sim 2.6$ , and  $\sim 5$  nm LSC<sub>214</sub> decorations, LSC<sub>113</sub> film with  $\sim 2.6$  nm LSC<sub>214</sub> decoration at 550 °C. (a) Nyquist plot of the epitaxial LSCF<sub>113</sub> and the epitaxial LSC<sub>214</sub>-decorated LSCF<sub>113</sub> films in 1 atm. (b) Nyquist plot of the LSCF<sub>113</sub> thin film with  $\sim 5$  nm LSC<sub>214</sub> coverage as a function of  $p(O_2)$ . (c) Oxygen partial pressure dependency of the surface exchange coefficients ( $k^a$ ) of the LSCF<sub>113</sub>, LSC<sub>113</sub>, LSC<sub>214</sub>-decorated LSCF<sub>113</sub>, LSC<sub>214</sub>-decorated LSC<sub>113</sub> films calculated from EIS spectra collected at 550

°C. Extrapolated bulk  $k^*$  (approximately equivalent to  $k^q$ ) values at 550 °C obtained from previous data of (☆-light blue) Steele et al.<sup>50</sup> and (★-light blue) De souza et al.<sup>6</sup> are plotted for comparison. (d) Oxygen partial pressure dependency of volume specific capacitance ( $VSC$ ) of the epitaxial LSCF<sub>113</sub>, LSC<sub>113</sub>, LSC<sub>214</sub>-decorated LSCF<sub>113</sub>, and LSC<sub>214</sub>-decorated LSC<sub>113</sub> films calculated from EIS spectra collected at 550 °C.

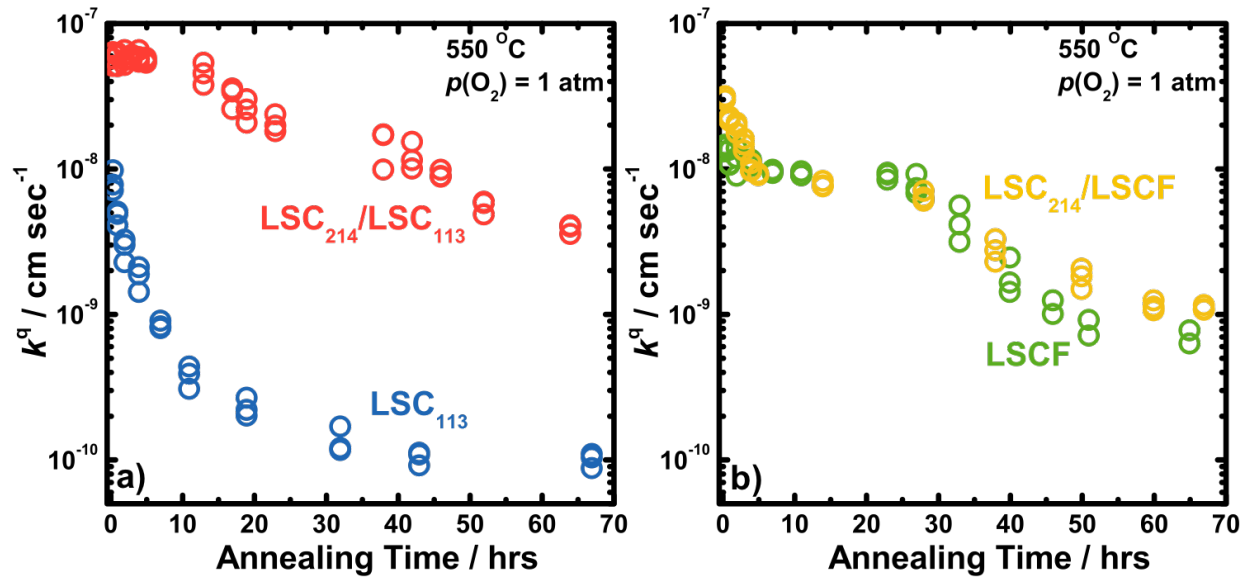


Fig. 3. Surface exchange coefficient ( $k^a$ ) of microelectrodes ( $\sim 200\text{ }\mu\text{m}$ ) for (a) the LSC<sub>113</sub> with and without LSC<sub>214</sub> coverage and (b) the LSCF<sub>113</sub> with and without LSC<sub>214</sub> coverage as a function of annealing time. Annealing was performed at  $550\text{ }^\circ\text{C}$  in an oxygen partial pressure of 1 atm. Three microelectrodes from each sample were measured at the same annealing time.

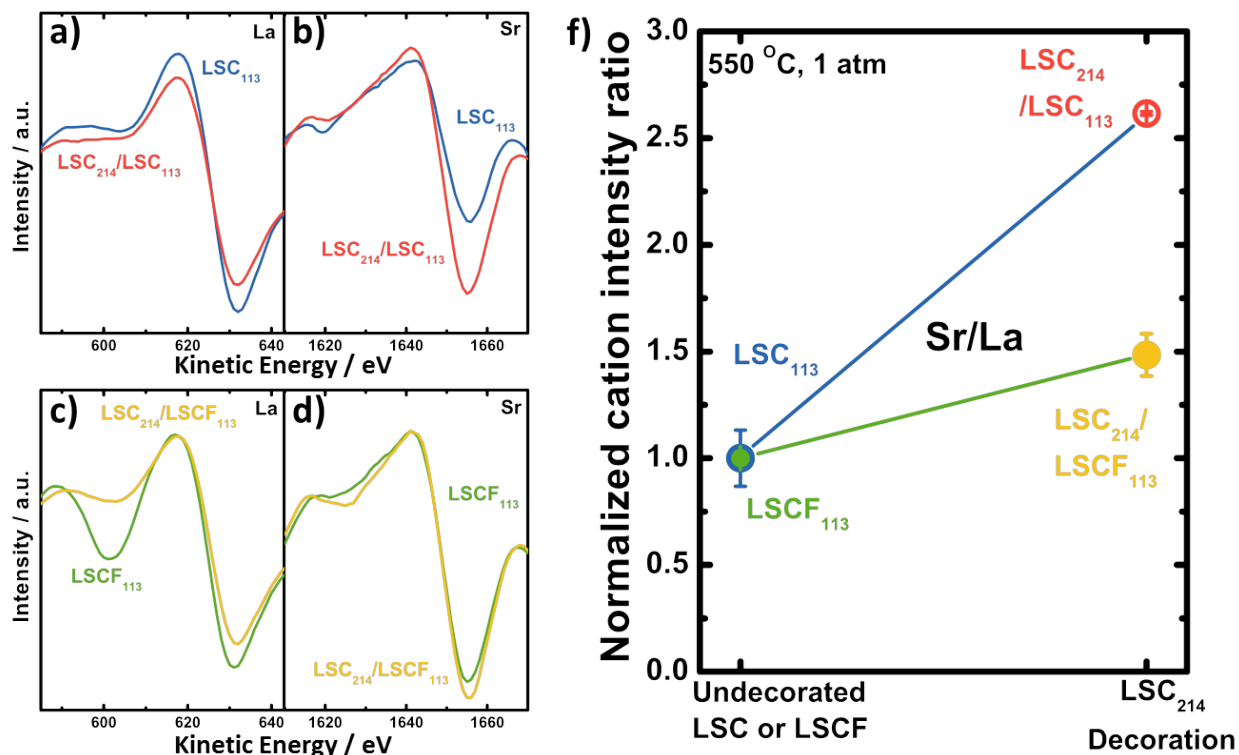


Fig. 4. Auger electron spectroscopy (AES) data from area mode for the LSCF<sub>113</sub> (green), LSC<sub>113</sub> (blue), LSCF<sub>113</sub> film with  $\sim 2.6$  nm LSC<sub>214</sub> decorations (yellow), and LSC<sub>113</sub> film with  $\sim 2.6$  nm LSC<sub>214</sub> decoration (red) after annealing. Annealing was performed at 550 °C for 6 hours in an oxygen partial pressure of 1 atm. (a) La Auger spectra and (b) Sr Auger spectra of the LSC<sub>113</sub> and LSC<sub>214</sub>-decorated LSC<sub>113</sub> films. (c) La Auger spectra and (d) Sr Auger spectra of the LSCF<sub>113</sub> and LSC<sub>214</sub>-decorated LSCF<sub>113</sub> films. (f) Normalized La and Sr intensity ratio extracted from AES of the LSCF<sub>113</sub> films with and without  $\sim 2.6$  nm LSC<sub>214</sub> decorations, and LSC<sub>113</sub> film with and without  $\sim 2.6$  nm LSC<sub>214</sub> decoration. Details of normalization methods are provided in the ESI †.

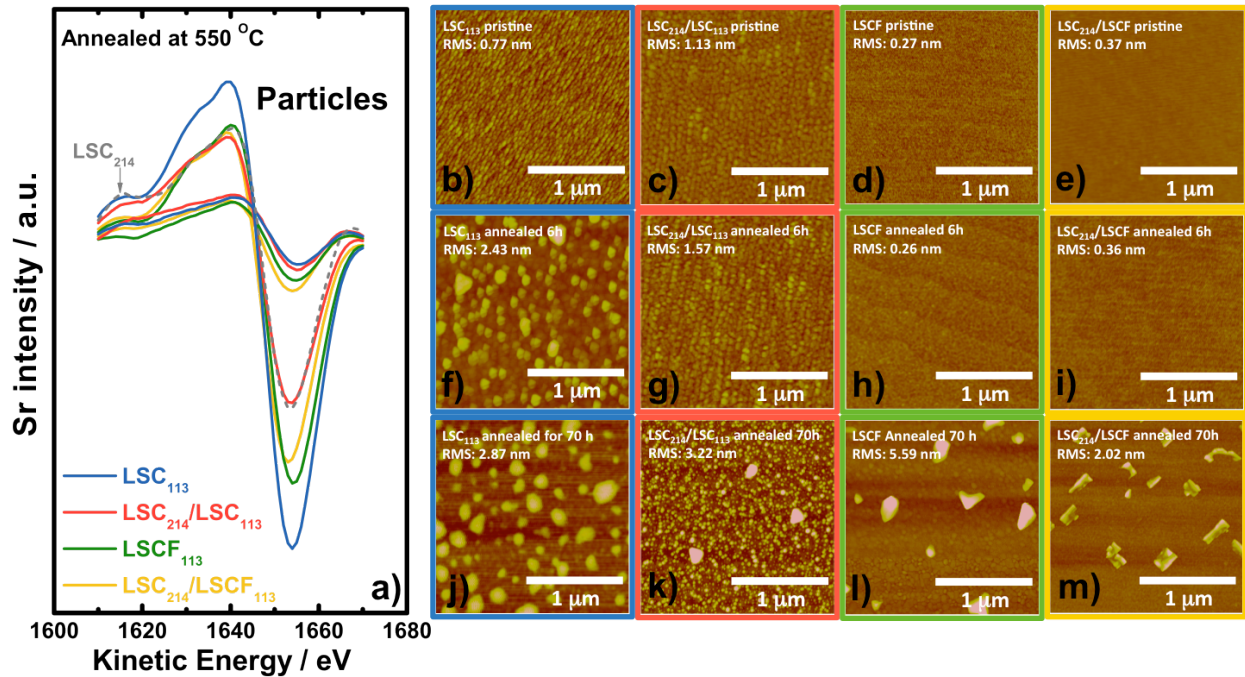
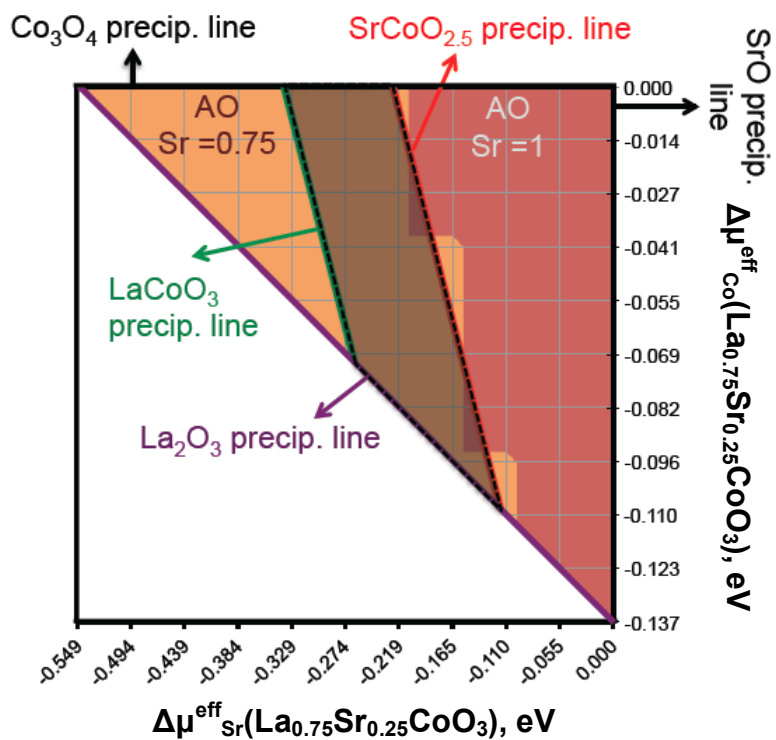


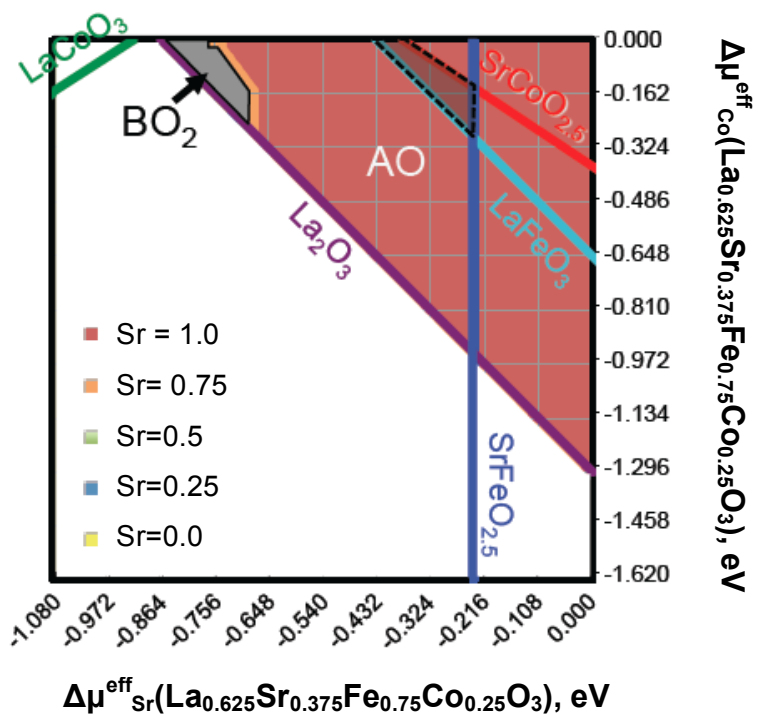
Fig. 5. Auger spectra and atomic force microscopy (AFM) images for bare LSC<sub>113</sub>, LSCF<sub>113</sub>, LSC<sub>214</sub>-decorated LSC<sub>113</sub>, and LSC<sub>214</sub>-decorated LSCF<sub>113</sub> thin films. (a) Sr Auger spectra for: LSC<sub>113</sub> (blue), LSC<sub>214</sub>-decorated LSC<sub>113</sub> (red), LSCF<sub>113</sub> (green), and LSC<sub>214</sub>-decorated LSCF<sub>113</sub> (yellow) after annealing at 550 °C for 70 hours in an oxygen pressure of 1 atm. The dashed gray line is the Sr spectra of a pristine LSC<sub>214</sub> reference sample. The peak-to-peak values in Auger spectra reflect the Sr concentrations. AFM images of as-deposited (b) LSC<sub>113</sub>, (c) LSC<sub>214</sub>-decorated LSC<sub>113</sub>, (d) LSCF<sub>113</sub>, and (e) LSC<sub>214</sub>-decorated LSCF<sub>113</sub>. AFM image showed particle formation on (f) 6 h annealed LSC<sub>113</sub> but no particles were observed on (g) 6 h annealed LSC<sub>214</sub>-decorated LSC<sub>113</sub>, (h) 6 h annealed LSC<sub>214</sub>-decorated LSC<sub>113</sub>, and (i) 6 h annealed LSC<sub>214</sub>-decorated LSC<sub>113</sub>. After annealing for 70 h, particles were observed on all surfaces; (j) annealed LSC<sub>113</sub>, (k) annealed LSC<sub>214</sub>-decorated LSC<sub>113</sub> (l) annealed LSCF<sub>113</sub> and (m) annealed LSC<sub>214</sub>-decorated LSCF<sub>113</sub>.

(a)



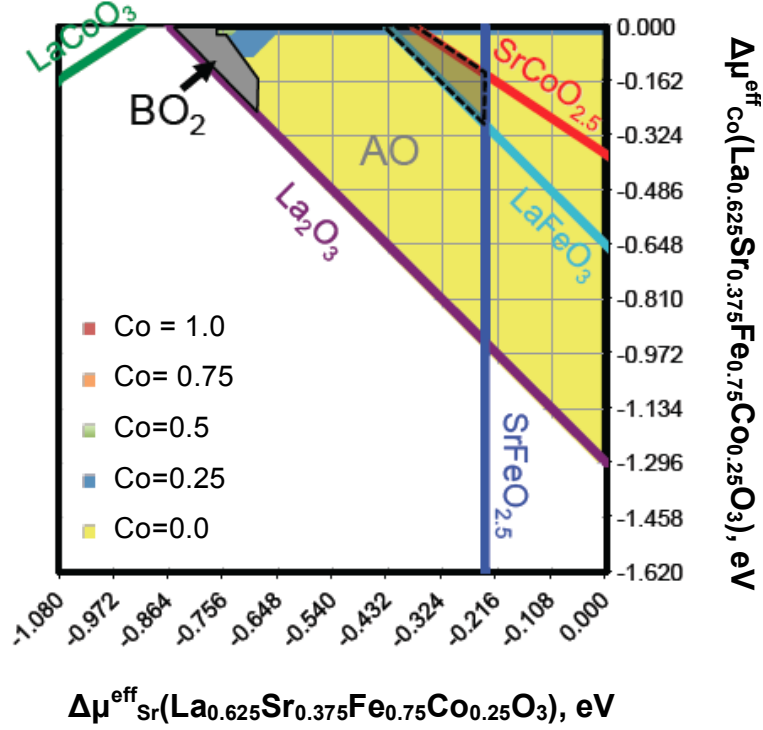
(b)

$\Delta\mu_{\text{Fe}}^{\text{eff}}(\text{La}_{0.625}\text{Sr}_{0.375}\text{Fe}_{0.75}\text{Co}_{0.25}\text{O}_3) = -0.12 \text{ eV vs. } \mu_{\text{Fe}}^{\text{eff}}(\text{Fe}_2\text{O}_3)$



(c)

$$\Delta\mu_{\text{Fe}}^{\text{eff}}(\text{La}_{0.625}\text{Sr}_{0.375}\text{Fe}_{0.75}\text{Co}_{0.25}\text{O}_3) = -0.12 \text{ eV vs. } \mu_{\text{Fe}}^{\text{eff}}(\text{Fe}_2\text{O}_3)$$



(d)

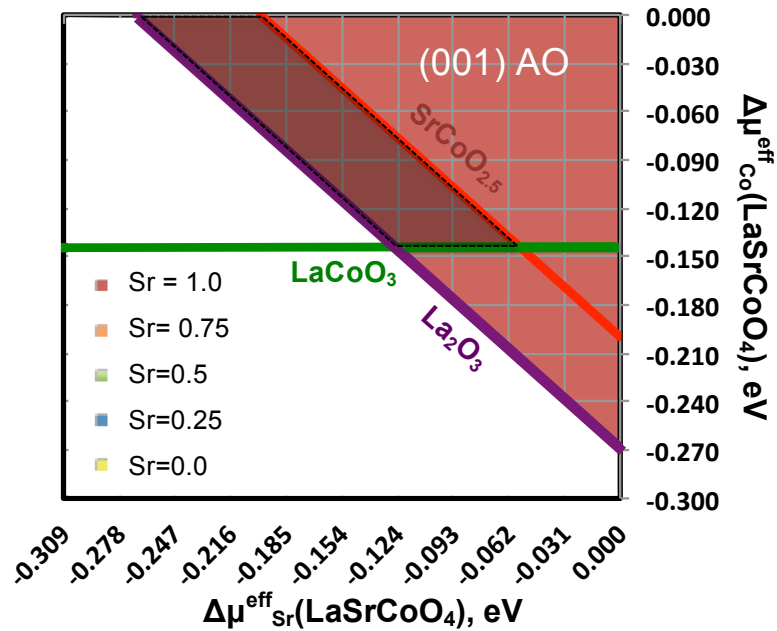


Fig. 6. Fig. 6a is the predicted  $\text{La}_{0.75}\text{Sr}_{0.25}\text{CoO}_3$  surface stability diagram at  $T = 550 \text{ }^\circ\text{C}$  and  $p(\text{O}_2) = 1 \text{ atm}$  based on the effective metal chemical potentials of bulk  $\text{La}_{0.75}\text{Sr}_{0.25}\text{CoO}_3$ . The grid points

represent the sampled bulk effective chemical potentials of Sr (x-axis; x=0 represents the equilibrium between  $\text{La}_{0.75}\text{Sr}_{0.25}\text{CoO}_3$  and SrO) and Co (y-axis; y=0 represents the equilibrium between  $\text{La}_{0.75}\text{Sr}_{0.25}\text{CoO}_3$  and  $\text{Co}_3\text{O}_4$ ) in  $\text{La}_{0.75}\text{Sr}_{0.25}\text{CoO}_3$ , and the contour plot beyond the grid is constructed based on the calculated lowest surface energy among the investigated  $\text{La}_{0.75}\text{Sr}_{0.25}\text{CoO}_3$  (001) surface configurations. The shaded area within dotted lines represents the  $\text{La}_{0.75}\text{Sr}_{0.25}\text{CoO}_3$  bulk stable region relative to the lower order oxide compounds ( $\text{LaCoO}_3$ –green,  $\text{SrCoO}_{2.5}$ –red,  $\text{La}_2\text{O}_3$ –purple,  $\text{SrO}$ –x=0, and  $\text{Co}_3\text{O}_4$ –y=0), the surface energy results are provided in Table S2†. The  $\text{La}_{0.75}\text{Sr}_{0.25}\text{CoO}_3$  (001) surface stability analysis results suggest the most stable surfaces are the AO surfaces with the surface layer A-site Sr concentration equal to 0.75 within the bulk stable region relative to the lower order oxide compounds. Fig. 6b and c are the predicted  $\text{La}_{0.625}\text{Sr}_{0.375}\text{Fe}_{0.75}\text{Co}_{0.25}\text{O}_3$  (001) top two surface layer Sr and Co composition at T = 550 °C and  $p(\text{O}_2) = 1$  atm at the condition of  $\Delta\mu_{\text{Fe}}^{\text{eff}}(\text{La}_{0.625}\text{Sr}_{0.375}\text{Fe}_{0.75}\text{Co}_{0.25}\text{O}_3) = -0.12$  eV vs.  $\mu_{\text{Fe}}^{\text{eff}}(\text{Fe}_2\text{O}_3)$ . The grid points represent the sampled bulk effective chemical potentials of Sr (x-axis; x=0 represents the equilibrium between  $\text{La}_{0.625}\text{Sr}_{0.375}\text{Fe}_{0.75}\text{Co}_{0.25}\text{O}_3$  and SrO) and Co (y-axis; y=0 represents the equilibrium between  $\text{La}_{0.625}\text{Sr}_{0.375}\text{Fe}_{0.75}\text{Co}_{0.25}\text{O}_3$  and  $\text{Co}_3\text{O}_4$ ) in  $\text{La}_{0.625}\text{Sr}_{0.375}\text{Fe}_{0.75}\text{Co}_{0.25}\text{O}_3$ . The effective chemical potential conditions in which the  $\text{BO}_2$  surface is more stable than the AO are presented by the grey area. The shaded area within dotted lines in Fig. 6b and 6c represents the  $\text{La}_{0.625}\text{Sr}_{0.375}\text{Fe}_{0.75}\text{Co}_{0.25}\text{O}_3$  bulk stable region relative to the lower order oxides ( $\text{LaFeO}_3$ –light blue,  $\text{SrFeO}_{2.5}$ –deep blue,  $\text{LaCoO}_3$ –green,  $\text{SrCoO}_{2.5}$ –red,  $\text{La}_2\text{O}_3$ –purple,  $\text{SrO}$ –x=0, and  $\text{Co}_3\text{O}_4$ –y=0). The  $\text{La}_{0.625}\text{Sr}_{0.375}\text{Fe}_{0.75}\text{Co}_{0.25}\text{O}_3$  (001) surface stability analysis results suggest the most stable surfaces are the AO surfaces with the surface layer A-site Sr concentration equal to 1.00 and such conclusion holds for all the other investigated conditions of  $\Delta\mu_{\text{Fe}}^{\text{eff}}(\text{La}_{0.625}\text{Sr}_{0.375}\text{Fe}_{0.75}\text{Co}_{0.25}\text{O}_3)$ , including  $\Delta\mu_{\text{Fe}}^{\text{eff}}(\text{La}_{0.625}\text{Sr}_{0.375}\text{Fe}_{0.75}\text{Co}_{0.25}\text{O}_3) = 0.0, -0.24, -$

0.36 eV vs.  $\mu_{\text{Fe}}^{\text{eff}}$  ( $\text{Fe}_2\text{O}_3$ ), as shown in Fig. S13a†, S13c†, and S13d†. Fig. 6d is the predicted contour plots for the  $\text{LaSrCoO}_4$  stable (001) vs. (100) surface layer compositions within the bulk  $\text{LaSrCoO}_4$  stability boundaries (in equilibrium with  $\text{La}_2\text{O}_3$ ,  $\text{SrO}$ ,  $\text{Co}_3\text{O}_4$ ,  $\text{LaCoO}_3$ , and  $\text{SrCoO}_{2.5}$ ) based on the most stable surface energy of the investigated six  $\text{LaSrCoO}_4$  (001) and (100) slab configurations (see Fig. S11† for more details) vs. chemical potentials of Sr (relative to  $\text{SrO}$ ) and Co (relative to  $\text{Co}_3\text{O}_4$ ) at  $T = 550$  °C and  $p(\text{O}_2) = 1$  atm. The shaded region represents the stable bulk  $\text{LaSrCoO}_4$ . For the same surface orientation, both the (001) AO and the (100)  $\text{A}_2\text{BO}_4$  surfaces are predicted to be stable with fully enriched surface layer Sr at the A-sites. Comparatively, the surface energy of the fully Sr-enriched (100)  $\text{A}_2\text{BO}_4$  surface is found to be a factor of 1.2 ~ 2 with respect to the surface energy of the fully Sr-enriched (001) AO surface within the stable bulk  $\text{LaSrCoO}_4$  region, suggesting the greater stability of the (001) AO surface with fully enriched Sr vs. the (100)  $\text{A}_2\text{BO}_4$  surfaces. Details of the *ab initio* thermodynamic analysis, definition of the effective chemical potentials, and additional information regarding to the sub-surface layer B-site composition, are provided in the ESI†.

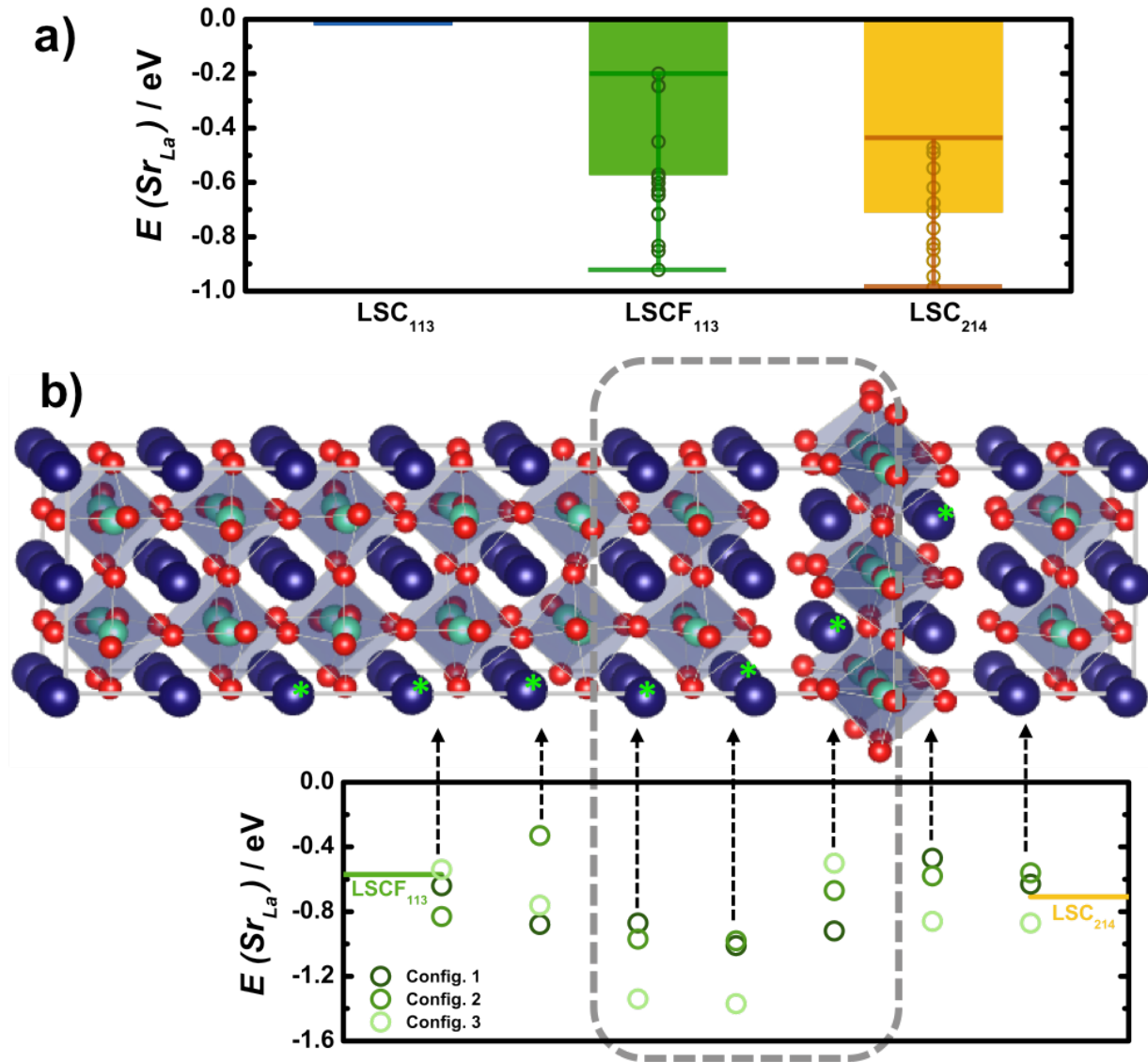


Fig. 7. (a) The calculated  $\text{Sr}_{\text{La}}$  substitution energies in bulk  $\text{LSC}_{214}$ ,  $\text{LSC}_{113}$ , and  $\text{LSCF}_{113}$  (all relative to that of  $\text{LSC}_{113}$ , which is set to 0). The error bars shown in the  $\text{LSCF}_{113}$  and  $\text{LSC}_{214}$  represent the upper bound and lower bound of the  $\text{Sr}_{\text{La}}$  substitution energies from the sampled A-site and B-site cation arrangements, and the values are calculated based on the difference in the calculated total energies between a  $\text{La}_{0.625}\text{Sr}_{0.375}\text{CoO}_3$  ( $\text{La}_{0.5}\text{Sr}_{0.5}\text{Fe}_{0.75}\text{Co}_{0.25}\text{O}_3$ ) bulk and a  $\text{La}_{0.75}\text{Sr}_{0.25}\text{CoO}_3$  ( $\text{La}_{0.625}\text{Sr}_{0.375}\text{Fe}_{0.75}\text{Co}_{0.25}\text{O}_3$ ) bulk. Similarly, the  $\text{Sr}_{\text{La}}$  substitution energy for  $\text{LSC}_{214}$  was calculated using the total energy difference between  $\text{LSC}_{214}$  and

( $\text{La}_{0.4375}\text{Sr}_{0.5625}$ ) $_2\text{CoO}_4$ ). (b) The heterostructured interface model used in the DFT simulations and the results of  $\text{Sr}_{\text{La}}$  substitution energies. Elements are represented as: La/Sr (dark blue), Fe/Co (light blue, center of the octahedra), and O (red). The dashed rounded rectangle represents an interfacial region. The relative stability of  $\text{Sr}_{\text{La}}$  substitution energy relative to  $\text{La}_{0.75}\text{Sr}_{0.25}\text{CoO}_3$ , or  $E(\text{Sr}_{\text{La}})$  of heterointerface -  $E(\text{Sr}_{\text{La}})$  of  $\text{LSC}_{113}(25\%\text{Sr})$ , is shown for the  $\text{Sr}_{\text{La}}$  substitution position in different AO planes labeled with asterisk(\*). Values are relative to a bulk  $\text{LSC}_{113}(25\%\text{Sr})$  reference ( $y=0$ ). Also shown is a yellow horizontal line representing the  $\text{Sr}_{\text{La}}$  substitution energies for the bulk  $\text{LSCF}_{113}$  ( $E(\text{Sr}_{\text{La}})$  of  $\text{LSCF}_{113}$  -  $E(\text{Sr}_{\text{La}})$  of  $\text{LSC}_{113}(25\%\text{Sr})$ ), and a orange line for the bulk  $\text{LSC}_{214}$  (or  $E(\text{Sr}_{\text{La}})$  of  $\text{LSC}_{214}$  -  $E(\text{Sr}_{\text{La}})$  of  $\text{LSC}_{113}(25\%\text{Sr})$ ). Note that the more negative values on the y-axis correspond to the easier substitution of the  $\text{Sr}_{\text{La}}$  relative to bulk  $\text{LSC}_{113}(25\%\text{Sr})$ , and three A-site and B-site cation arrangements in the heterostructured interface models are explored to calculate the  $\text{Sr}_{\text{La}}$  substitution energy relative to  $\text{La}_{0.75}\text{Sr}_{0.25}\text{CoO}_3$  (See Fig. S9† for more details on the DFT modeling).

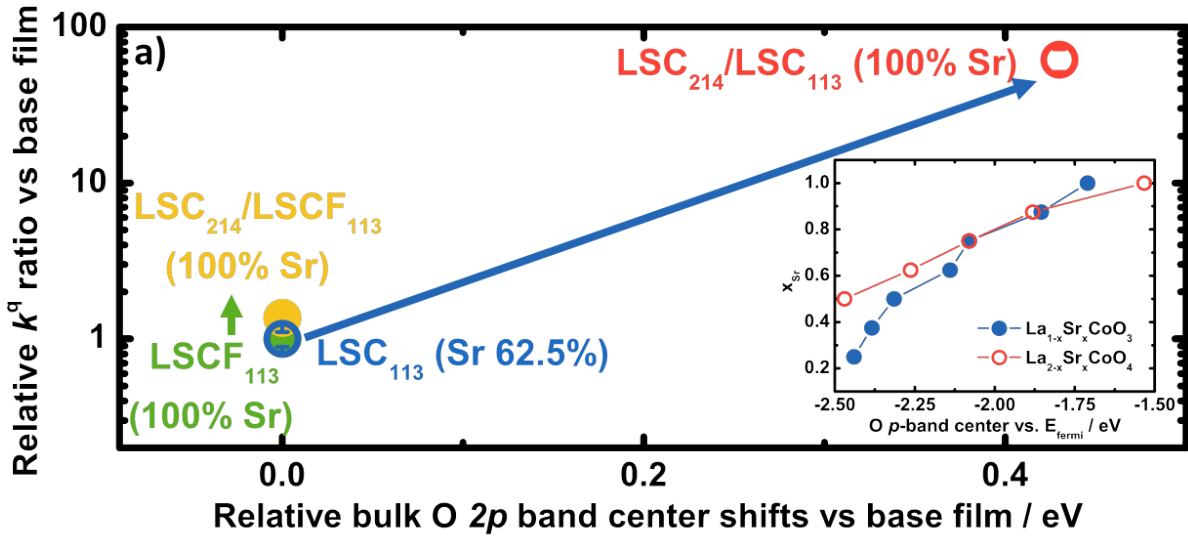
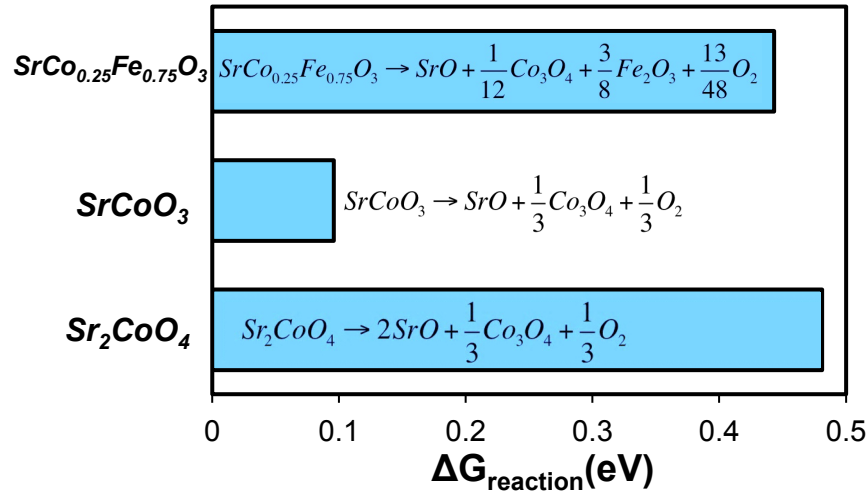


Fig. 8. (a) The relative ratio of the surface exchange coefficient  $k^q$  (with respect to the  $k^q$  of the base film) vs. the calculated bulk O  $2p$  band center shifts (relative to the Fermi level) between the  $\text{LSC}_{214}$ -decorated  $\text{LSCF}_{113}$  ( $\text{LSC}_{113}$ ) film surfaces and the undecorated  $\text{LSCF}_{113}$  ( $\text{LSC}_{113}$ ) film surfaces based on the surface Sr information from COBRA analysis<sup>63</sup> and DFT modeling predictions. The inset shows the Sr content vs the calculated bulk O  $2p$  band centers of  $\text{LSC}_{113}$  and  $\text{LSC}_{214}$ .

(a)



(b)

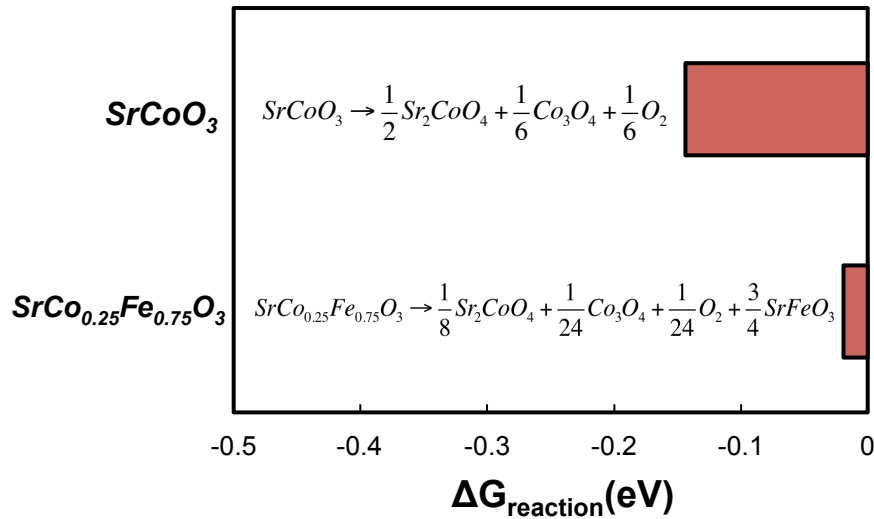


Fig. 9. (a) The decomposition reaction free energy to form the lower order binary metal oxides of fully Sr enriched LSCF<sub>113</sub>, LSC<sub>113</sub>, and LSC<sub>214</sub>. (b) The decomposition reaction free energy to form Sr<sub>2</sub>CoO<sub>4</sub> and lower order transition metal binary metal oxides of fully Sr enriched LSC<sub>113</sub> and LSCF<sub>113</sub>, both at T = 550 °C and  $p(\text{O}_2) = 1 \text{ atm}$ . We note that an additional B-site configuration entropy term for SrCo<sub>0.25</sub>Fe<sub>0.75</sub>O<sub>3</sub>, which corresponds to -0.04 eV per formula unit and will further stabilize the SrCo<sub>0.25</sub>Fe<sub>0.75</sub>O<sub>3</sub>, is neglected in both Fig. 9 (a) and (b).